Subcellular spatial transcriptomics identifies three mechanistically different classes of localizing RNAs

Lucia Cassella[1,2] and Anne Ephrussi[1]*

[1]European Molecular Biology Laboratory, Meyerhofstrasse 1, Heidelberg, 69117, Germany

[2]Collaboration for joint PhD degree between EMBL and Heidelberg University, Faculty of Biosciences

*corresponding author, anne.ephrussi@embl.org

1 **Abstract**

2 Intracellular RNA localization is a widespread and dynamic phenomenon that compartmentalizes gene

3 expression and contributes to the functional polarization of cells. Thus far, mechanisms of RNA

4 localization identified in *Drosophila* have been based on a few RNAs in different tissues, and a

5 comprehensive mechanistic analysis of RNA localization in a single tissue is lacking. Here, by

6 subcellular spatial transcriptomics we identify RNAs localized in the apical and basal domains of the

7 columnar follicular epithelium (FE) and we analyze the mechanisms mediating their localization.

8 Whereas the dynein/BicD/Egl machinery controls apical RNA localization, basally-targeted RNAs

9 require kinesin-1 to overcome a "default" dynein-mediated transport. Moreover, a non-canonical,

10 translation- and dynein-dependent mechanism mediates apical localization of a subgroup of dynein-

11 activating adaptor RNAs (*BicD*, *Bsg25D*, *hook*). Altogether, our study identifies at least three

12 mechanisms underlying RNA localization in the FE, and suggests a possible link between RNA

13 localization and dynein/dynactin/adaptor complex formation *in vivo*.

14

INTRODUCTION

RNA localization allows the precise compartmentalization of gene expression in space and time, and is a widespread phenomenon in many different cell types and organisms (Shepard et al., 2003; Blower et al., 2007; Lécuyer et al., 2007; Mili et al., 2008; Jambor et al., 2015; Wilk et al., 2016; Moor et al., 2017). Three main mechanisms have been described to account for RNA localization: (1) active transport on cytoskeletal tracks, (2) localized protection from degradation, or (3) facilitated diffusion and entrapment (Medioni et al., 2012). Recently, several novel mechanisms have been reported to mediate RNA localization, such as hitch-hiking on other RNAs or organelles and co-translational RNA transport (Corradi et al., 2020; Cioni et al., 2019; Liao et al., 2019; Baumann et al., 2014; Harbauer et al., 2021; Cohen et al., 2021; Sepulveda et al, 2018). Active transport is the best characterized mode of RNA localization and consists in the transport of ribonucleoprotein particles by motor proteins on cytoskeletal tracks. Localizing RNAs are typically transported in a translationally silent state and encode cis-acting localization elements (LEs) that are recognized and bound by trans-acting RNA-binding proteins (RBPs) mediating motor recruitment (Xing & Bassell, 2013).

Kinesin motor proteins mostly mediate microtubule (MT) plus end-directed transport. Kinesin-1 (Khc) has been shown to mediate *oskar* (*osk*) RNA localization to the posterior pole of the *Drosophila* oocyte (Brendza et al., 2000; Zimyanin et al., 2008). Whereas Tropomyosin-1 isoform I/C (atypical Tm1, *a*Tm1) regulates *osk* posterior localization by directly stabilizing Khc interaction with the RNA (Dimitrova-Paternoga et al., 2021; Gáspár et al., 2016; Erdélyi et al., 1995), the Exon Junction Complex (EJC) deposited upon splicing is thought to activate kinesin-1 transport of the RNA (Gáspár et al., 2016). Little is known about MT plus end-directed RNA transport in other tissues. Interestingly, *a*Tm1 is also important for *coracle* RNA localization at *Drosophila* neuromuscular junctions (Gardiol & St Johnston, 2014) and the EJC has been shown to mediate *NIN* RNA localization in human RPE1 cells (Kwon et al., 2021).

Cytoplasmic dynein and its accessory complex dynactin direct trafficking of cargoes towards MT minus ends. In *Drosophila*, dynein-mediated RNA transport is accomplished by the dynein-activating adaptor Bicaudal-D (BicD) and the RNA binding protein Egalitarian (Egl) (Mach & Lehmann, 1997; Navarro et al., 2004; Dienstbier et al., 2009). The dynein/BicD/Egl complex is thought to mediate

45   nurse cell-to-oocyte transport of maternal RNAs, and was shown to direct apical RNA localization in

46   the early embryo, neuroblasts, and polar cells (Clark et al., 2007; Wilkie & Davis, 2001; Bullock & Ish-

47   Horowicz, 2001; Hughes et al., 2004; Van De Bor et al., 2011). The dynein/dynactin/BicD (DDB) motor

48   complex is highly conserved and participates in the transport of different cargoes, with BicD (and its

49   mammalian ortholog BICD2) linking the dynein motor to specific cargoes. While proteins binding to the

50   BicD C-terminal domain (CTD), such as Egl or Rab6, impart cargo specificity (Matanis et al., 2002;

51   Hoogenraad et al., 2003; Dienstbier et al., 2009; Coutelis & Ephrussi 2007; Januschke et al., 2007),

52   the BicD N-terminal domain (corresponding to coiled-coil 1/2, CC1/2) binds to dynein/dynactin

53   (Hoogenraad et al., 2001, 2003) and activates dynein processivity (McKenney et al., 2014; Schlager et

54   al., 2014; Dienstbier et al., 2009; Sladewski et al., 2018).

55

56   Although much of what is known about RNA localization comes from studies of maternally inherited

57   RNAs in the *Drosophila* germline, several examples of localizing RNAs have been also reported in the

58   follicular epithelium (FE) that envelops the germline cyst (Jambor et al., 2015; Li et al., 2008; Horne-

59   Badovinac & Bilder, 2008; Vazquez-Pianzola et al., 2017; Schotman et al., 2008; Serano & Rubin,

60   2003). The FE is composed of highly polarized secretory follicle cells (FCs) belonging to the somatic

61   lineage, with minus ends of non-centrosomal microtubules (ncMTs) anchored at the apical cell cortex

62   facing the oocyte (Clark et al., 1997; Khanal et al., 2016). The FE is an easily manipulatable and

63   powerful genetic system that, through the generation of mosaics, allows the dissection of the effect of

64   mutations without disrupting developmental processes. Several lines of evidence indicate that the

65   dynein/BicD/Egl RNA transport complex active in nurse cell-to-oocyte transport is also responsible for

66   the apical localization of a handful of RNAs in the FE (Li et al., 2008; Bhagavatula & Knust, 2021;

67   Karlin-McGinness et al., 1996; Jambor et al., 2014; Vazquez-Pianzola et al., 2017; Van De Bor et al.,

68   2011). However, a comprehensive overview of RNA localization in the FE and its underlying

69   mechanisms are lacking.

70

71   Here, we apply subcellular spatial transcriptomics to first identify the landscape of apically- and

72   basally-localizing RNAs in the columnar FE. By screening a subset of apical and basal RNAs identified

73   in this way, we find that the dynein/BicD/Egl machinery acts by "default" in directing apical RNA

74   localization, and that an additional kinesin-1-dependent layer of regulation must be applied to direct

75   basal RNA localization. Moreover, we identify a third, translation- and dynein-dependent mechanism

76   that underlies the apical localization of transcripts encoding dynein-activating adaptors, providing a

77   possible link between RNA localization and dynein/dynactin/adaptor complex formation *in vivo*.

78

RESULTS

Identification of apical and basal RNAs in columnar follicle cells

To identify RNAs that localize apically or basally in *Drosophila* FE transcriptome-wide, we applied laser-capture microdissection (LCM) to isolate fragments of tissue that consisted in either the apical half ("apical domain") or basal half ("basal domain") of adjacent columnar follicle cells (**Figure 1A and Movie S1**). Differential gene expression analysis of apical vs. basal LCM-derived RNA-seq samples yielded 306 RNAs enriched in the apical samples and 249 RNAs enriched in the basal samples (false discovery rate [FDR] < 0.1) (**Figure 1B**). Since LCM is highly susceptible to tissue contamination, we first aimed at identifying those RNAs whose significant enrichment was a result of contamination by other cell types, such as the oocyte on the apical side or the circular muscles on the basal side (**Figure S1A**). To do so, we analyzed those RNAs characterized by high absolute log2-transformed fold change (|log2FC|) values of apical over basal abundance that might result from contamination of neighboring tissues expressing a different set of hallmark genes. By setting an arbitrary threshold of |log2FC| > 3 as indicative of contaminant RNA identity, we found 33 putative basal contaminants of muscle origin (log2FC < -3) and 2 putative apical contaminants of oocyte origin (log2FC > 3) (**Figure 1B** and **Figure S1B**). 2/3 (n=22) of basal genes with log2FC < -3 were annotated as being expressed or having a function in muscle tissues (FlyBase) and their mapped reads were often absent or in very low number in the apical fragments (**Figure S1C,D**). Moreover, we validated through single molecule Fluorescence *In Situ* Hybridization (smFISH) 3 putative basal contaminants (*Mhc*, *Act57B*, *wupA*) as being enriched in circular muscles with little or no expression in the FE (**Figure S1E**). This analysis resulted in 304 *bona fide* apical RNAs and 216 *bona fide* basal RNAs localizing in the columnar FE (**Figure 1B, Table S1**). Finally, 16 RNAs were randomly chosen from the computationally established list of significantly enriched *bona fide* apical or basal RNAs and were validated as true localizing RNAs through smFISH (**Figure 1C**).

Basal RNA localization depends on kinesin-1, *a*Tm1, and the EJC

Basal RNA localization is a largely uncharacterized phenomenon. Previous reports have identified a limited number of basally-localizing RNAs in the FE (Jambor et al., 2015; Schotman et al., 2008; Serano & Rubin, 2003), with little mechanistic insight. For this reason, we sought to elucidate the

6

109   mechanisms behind basal RNA localization. Early reporter-based studies on the polarity of *Drosophila*

110   tissues have shown that the basal domain of the FE is functionally equivalent to the posterior pole of

111   the oocyte, as both compartments accumulate the MT plus end marker Kin:βgal (Clark et al., 1997).

112   Therefore, we hypothesized that the regulators of *oskar* posterior RNA transport might also be

113   responsible for basal RNA localization in the FE. To test this hypothesis, we disrupted known

114   components of the *osk* RNP transport machinery, such as kinesin-1 (Khc), atypical Tropomyosin-1

115   (*a*Tm1) and the Exon Junction Complex (EJC) (**Figure S2A**) in the FE and analyzed the localization

116   pattern of 4 validated basal RNAs (*Fkbp14*, *CG3308*, *Rtnl1*, *zip*) (**Figure 2**). In all cells lacking either

117   Khc (*Khc* RNAi cells) (**Figure 2A**), *a*Tm1 (*Tm1^{NULL}*, Erdélyi et al., 1995) (**Figure 2B**), or the EJC (*ΔC-*

118   *Pym* cells, Ghosh et al., 2014) (**Figure 2C**), basal RNA localization was severely disrupted, with all

119   basal RNAs analyzed becoming apically localized. To check whether the changes observed in RNA

120   localization were specific of basal RNAs, we analyzed the localization pattern of 4 apical RNAs

121   validated previously (*crb*, *msps*, *qtc*, *CG33129*) in the same mutants. In contrast to basal RNAs, none

122   of the apical RNAs analyzed were affected by disruption of kinesin-1-mediated RNA transport (**Figure**

123   **S2B-D**), indicating that regulators of RNA transport towards MT plus ends specifically control basal

124   RNA localization. To have a quantitative overview of changes in RNA localization, we considered the

125   ratio between the apical and the basal smFISH signal intensity in either wild-type (wt) or knock-down

126   (KD) cells, and called this parameter Degree of Apicality (DoA), as values > 1 indicate an apical

127   localization bias. Then, we tested whether the DoA values of each RNA analyzed significantly differ in

128   KD vs. wt cells by calculating the ratio between the DoA(KD) and the DoA(wt) for each RNA in each of

129   the 3 conditions (see Materials and Methods and Figure 2 for statistical testing). With this analysis, we

130   confirmed that (1) all basal RNAs were affected by lack of Khc, *a*Tm1, or EJC and (2) none of the

131   apical RNAs significantly changed localization pattern upon knock-down of kinesin-1 regulators

132   (**Figure 2D**), showing that kinesin-1, *a*Tm1, and the EJC are specifically responsible for basal RNA

133   localization in the FE.

134

135   **Mislocalization of the basal RNA *zip* depends on Egalitarian**

136   Interestingly, upon disruption of MT plus end-directed RNA transport all analyzed basal RNAs were

137   mislocalized to the apical domain. Several studies reported that apical RNA localization depends on

138   the BicD/Egl machinery, a dynein-dependent complex that localizes RNAs apically in the blastoderm

139 embryo and is thought to be responsible for nurse cell-to-oocyte transport of maternal RNAs.

140 Therefore, the apical mislocalization of basal RNAs observed upon knock-down of kinesin-1 regulators

141 might be due to apical RNA transport by the dynein/BicD/Egl machinery. To test this, we generated FC

142 clones lacking either Egl (*egl* RNAi) or Khc (*Khc* RNAi), or both Egl and Khc [(*egl+Khc*) RNAi] and

143 evaluated changes in the RNA localization of *zip*, one of the most striking examples of the apical

144 mislocalization phenomenon (see Figure 2A-C). Whereas *zip* RNA was unaffected upon *egl* RNAi and

145 strongly apically mislocalized in *Khc* RNAi conditions as also highlighted by our previous experiments,

146 (*egl+Khc*) RNAi caused *zip* to assume a ubiquitous localization that would be consistent with a failure

147 of both kinesin-1-and dynein-mediated transport (**Figure S3A**). *zip* DoA measurements in wt and *RNAi*

148 cells in each of the three conditions provided a quantitative evaluation of the changes observed in

149 smFISH experiments (**Figure S3B**), with a significant decrease in KD/wt DoA in double (*egl+Khc*)

150 RNAi cells (KD/wt DoA = 1.61) compared to *Khc* RNAi cells (KD/wt DoA = 2.49) (**Figure S3C**).

151 Therefore, despite being dispensable in basal RNA localization under normal conditions, the

152 dynein/BicD/Egl complex is responsible for the apical mislocalization of a basal RNA (and possibly

153 more) when kinesin-1 activity is lacking.

154

155 **Two different dynein-dependent mechanisms control apical RNA localization**

156 As mentioned previously, several reports have identified the dynein/BicD/Egl machinery as

157 responsible for the apical localization of a subset of RNAs in the FE, such as *crumbs* (*crb*) (Li et al.,

158 2008; Bhagavatula & Knust, 2021). To test in an unbiased way the degree of involvement of the

159 dynein/BicD/Egl machinery in the localization of apical RNAs in the FE, we generated FC mutant

160 clones in which either cytoplasmic dynein (*Dhc64C*, hereafter called *Dhc*) or Egalitarian (*egl*) were

161 knocked-down by RNAi (**Figure S4A**). We then analyzed the localization pattern of 5 validated apical

162 RNAs (*crb*, *msps*, *qtc, CG33129, BicD*, with *crb* RNA as a positive control) by smFISH, along with the

163 quantification of RNA localization by measuring the KD/wt DoA. The localization of all apical RNAs

164 analyzed was completely abolished when *Dhc* was knocked down by RNAi, with the RNAs becoming

165 ubiquitously distributed (**Figure 3A,C**). *egl* RNAi caused all apical RNAs to lose their apical

166 localization, with the surprising exception of *BicD* (**Figure 3B,C**; see below). In contrast, basal RNAs

167 largely maintained their basal localization pattern upon either *Dhc* RNAi or *egl* RNAi treatment (**Figure**

168 **S4B,C** and **Figure 3C**). Basal RNA localization was only mildly affected in a subset of *Dhc* RNAi cells,

8

169   likely as a consequence of the emergence of polarity defects in cells lacking Dhc (Horne-Badovinac &

170   Bilder, 2008; Ronchi et al, 2021) (see Figure 3A and Figure S3B). The maintenance of *BicD* RNA

171   localization in *egl* RNAi cells was not due to a low efficiency of the RNAi, since both *egl* RNA and Egl

172   protein were significantly reduced in *egl* KD cells (**Figure S4D,E**). Moreover, in egg chambers entirely

173   lacking Egl throughout the FE (*egl^{NULL}FC*, see Materials and Methods), *BicD* RNA was still apically

174   localized, whereas localization of *CG33129* RNA, previously found to be Egl-dependent (see Figure

175   3B), was disrupted (**Figure S4F**). Altogether, these results show that the dynein/BicD/Egl complex is

176   largely responsible for apical RNA localization, but a different dynein-dependent mechanism underlies

177   the apical localization of *BicD* RNA. Considering that the Egl-independent targeting of *BicD* RNA

178   represents a novel mechanism of apical RNA localization, we sought to gain more insight into the

179   mechanisms regulating its RNA transport.

180

181   ***BicD* RNA localization requires an intact translation machinery**

182   Localization of *BICD2/BicD* RNA at centrosomes in cultured cells is translation-dependent (Safieddine

183   et al., 2021). To test whether *BicD* RNA localization in the FE involves the same mechanism, we

184   treated egg chambers *ex vivo* with the translation inhibitors puromycin (Puro) and cycloheximide

185   (CHX) and analyzed the distribution of *BicD* RNA under these two conditions compared to control

186   ovaries incubated in Schneider's medium only (**Figure 4A**). To assess tissue integrity, in parallel we

187   visualized *osk* RNA, whose localization during the middle stages of oogenesis should not be affected

188   by translation inhibitors. Whereas the localization pattern of *BicD* RNA in CHX-treated egg chambers

189   was similar to controls (**Figure 4B,D**), Puro treatment clearly impaired *BicD* RNA localization in the FE

190   (**Figure 4C**). The distribution of *BicD* signal intensity along the A-B axis of mid-stage follicle cells

191   shows that *BicD* enrichment at the apical cortex of the FE was severely reduced upon Puro treatment

192   (**Figure 4E**). As a proxy for the degree of signal mislocalization, we calculated the value

193   corresponding to 50% of the cumulative area under the curve (a.u.c.) in Puro- or CHX-treated egg

194   chambers and compared it with untreated controls. The results of this analysis show that the *BicD*

195   RNA signal shifted significantly towards the basal domain in Puro-treated egg chambers, whereas

196   CHX had no effect on *BicD* RNA localization (**Figure 4F**). The fact that freezing elongating ribosomes

197   (CHX condition) does not affect *BicD* RNA localization, whereas blocking translation by releasing the

198   nascent peptide (Puro condition) does, indicates that an intact translation machinery and the presence

199   of a nascent peptide may be required for *BicD* RNA localization in FCs.

200

201   **BicD RNA is co-translationally localized**

202   To understand whether the localization of *BicD* depends on translation of its own RNA (in *cis*) or of

203   other factors (in *trans*), we designed a series of transgenic constructs consisting of a BicD-GFP

204   cassette inserted downstream of an 18-bp linker in which we could introduce the desired frameshift

205   mutations without disrupting any unknown RNA localization element in the BicD CDS (**Figure S5A**).

206   Each of these transgenes was expressed in FC clones in a *BicD* wild-type background and the

207   transgenic *BicD-GFP* RNA was specifically detected by smFISH using antisense GFP probes. *GFP*

208   RNA carrying the same 3' untranslated region (UTR) as BicD-GFP constructs failed to localize when

209   expressed in the germline or in the FE (**Figure S5B**), showing that this sequence alone is not

210   sufficient to drive RNA localization. In contrast, the in-frame ^{0}*BicD-GFP* RNA showed a strong apical

211   localization in FCs (**Figure 4G-I**), similarly to the endogenous *BicD* RNA (see Figure S6A). Moreover,

212   the expression of full-length BicD-GFP was validated by the presence of GFP fluorescence in CD8-

213   mCherry^{+} cells expressing the transgene (**Figure 4G**). Disruption of the BicD-GFP reading frame by

214   either +1 or -1 frameshift, verified by the absence of GFP signal in CD8-mCherry^{+} cells, was sufficient

215   to impair apical RNA localization (**Figure 4G-I**). Consistent with the puromycin-induced impairment of

216   RNA localization in the FE, these results show that *BicD* RNA is co-translationally localized at the

217   apical cortex.

218

219   **BicD and Dhc RNAs decorate dynein particles at the apical cortex**

220   As in BicD the first peptide emerging from the ribosome is the dynein-binding domain (Hoogenraad et

221   al., 2003), the co-translational localization of *BicD* RNA might depend on association of nascent BicD

222   protein with dynein. To have an indication whether this might be the case, we imaged *BicD* RNA by

223   smFISH in ovaries expressing endogenously tagged Dhc-GFP (Gaspar et al., 2021). Although the

224   Dhc-GFP signal was diffuse in the ovary, distinct Dhc-GFP foci were detected at the apical cortex of

225   columnar FCs (**Figure 4J**) and elsewhere in the germline (see below). These foci also contain *Dhc*

226   RNA, indicating that these might be sites of *Dhc* RNA translation. *BicD* RNA showed a partial co-

227   localization with Dhc-GFP/*Dhc* RNA foci, consistent with the hypothesis of its co-translational

228   association with newly synthesized Dhc protein at the apical cortex.

229

230   **The first step of *BicD* RNA localization in the early cyst is translation-independent**

231   In the germline, BicD has an instructive role in oocyte specification (Wharton & Struhl, 1989; Suter &

232   Steward, 1991; Mach & Lehmann, 1997). Importantly, *BicD* RNA localization reflects MT minus end

233   enrichment (Steinhauer & Kalderon, 2006; Clark et al., 1997) in both the germline and FE (**Figure**

234   **S6A**). We noticed that, as in the FE, *BicD* RNA localization to the posterior of the oocyte (stages 9-10)

235   was impaired in Puro-treated ovaries, whereas CHX had no effect (**Figure 4C,D**). The same effect

236   was visible in younger egg chambers, starting when BicD becomes posteriorly localized in the small

237   oocyte at stages 4-5 (**Figure S6B**). In contrast, neither Puro nor CHX treatment abolished *BicD* nurse

238   cell-to-oocyte transport in early egg chambers, with *BicD* enrichment in the small oocyte being close to

239   wild-type levels (**Figure S6B**). Consistent with this, germline-driven *Frameshift* BicD-GFP RNA

240   underwent nurse cell-to-oocyte transport and displayed a clear oocyte enrichment during early stages,

241   similarly to endogenous *BicD* (**Figure S6C**). However, within the oocyte, *Frameshift* RNA was

242   ubiquitously distributed at these stages, and failed to localize at the posterior cortex of the small

243   oocyte. These results indicate that the process of *BicD* RNA transport into the oocyte does not involve

244   active translation; on the other hand, *BicD* RNA localization within the oocyte is likely governed by the

245   same co-translational mechanism that operates in the FE. In support of this hypothesis, we found that

246   *BicD* RNA decorates Dhc/*Dhc* RNA foci in both the FE and the oocyte, but not in the nurse cells

247   (**Figure S6D**). Taken together, these results indicate that the mid-oogenesis oocyte and the columnar

248   FCs share a similar co-translational mechanism for *BicD* RNA localization. In contrast, *BicD* RNA

249   nurse cell-to-oocyte localization appears to be mediated by a translation-independent mechanism that

250   does not involve the association with Dhc/*Dhc* RNA particles.

251

252   **A subset of dynein-activating adaptor RNAs are also co-translationally localized in the FE**

253   BicD belongs to the class of dynein-activating adaptors, linking cargoes to the dynein motor complex

254   (Olenick & Holzbaur, 2019). We found that the RNA encoding all *Drosophila* orthologs of the currently

255   known or putative dynein activating adaptors (hereafter collectively called "adaptor RNAs"), namely

256   *hook* (HOOK2-3), *Bsg25D* (NIN/NINL), *Nuf* (RAB11FIP3), and *Milton* (TRAK1-2), were significantly

257   enriched apically in our list of localizing transcripts (**Table S1**), with the exception of *Spindly* (SPDL1)

258   which was below the detection threshold. By hypothesizing that the same dynein-dependent co-

259   translational process that drives *BicD* RNA localization would also be responsible for the apical

260   localization of adaptor RNAs, we tested whether the localization of adaptor RNAs was affected by

261   either *Dhc* or *egl* RNAi. With the exception of *Nuf* and *Milton*, whose localization was disrupted by

262   either treatment (data not shown), the apical localization of *Bsg25D* and *hook* (**Figure 5A**) was

263   significantly disrupted in *Dhc* RNAi cells (**Figure 5B,D**), but not in *egl* RNAi cells (**Figure 5C,D**).

264   Moreover, the apical localization of both adaptor RNAs showed sensitivity to Puro but not CHX

265   (**Figure 5E,F**), although the change measured in *Bsg25D* signal distribution along the A-B axis in the

266   FE was not significantly different from untreated control (**Figure 5G**). However, *Bsg25D* is expressed

267   at low levels in the FE, hindering a robust quantitative image analysis. To further investigate whether

268   *hook* and *Bsg25D* use the same localization mechanism as *BicD*, we analyzed their spatial

269   relationship with Dhc-GFP/*Dhc* RNA particles. As for *BicD*, both *Bsg25D* (**Figure 5H**) and *hook*

270   (**Figure 5I**) were shown to partially co-localize with, thus decorate Dhc-GFP foci, which also contain

271   *Dhc* RNA. Overall, these results suggest that the RNAs encoding the dynein activating adaptors *BicD*,

272   *hook*, and *Bsg25D*, represent a subgroup of apical RNAs that share the same co-translational, dynein-

273   dependent mechanism that ensures their localization at cortical dynein foci also containing *Dhc* RNA.

274

DISCUSSION

Only few examples of localizing RNAs in the FE have been described to date, with little mechanistic insight (Jambor et al., 2015; Li et al., 2008; Horne-Badovinac & Bilder, 2008; Vazquez-Pianzola et al., 2017; Schotman et al., 2008; Serano & Rubin, 2003). To explore the extent of RNA localization in a somatic tissue *in vivo* and gain insight into the mechanisms underlying the phenomenon, we have used laser-capture microdissection of apical and basal subcellular fragments of columnar follicle cells coupled with RNA-seq to identify localizing RNAs in this tissue. This allowed us to investigate in detail the landscape of mechanisms that mediate both apical and basal RNA localization in the FE (**Figure 6A**). In our study, we found that basal RNA localization is mechanistically analogous to posterior RNA localization in the oocyte (represented by *osk*), reflecting MT plus end enrichment (Clark et al., 1997). Khc, *a*Tm1, and the EJC appear to be core components of a general "basal" RNA localization machinery. These results are in line with previous findings on *osk* RNA indicating that Khc/*a*Tm1 bind to the 3'UTR (Gaspar et al., 2017) and the EJC activates kinesin-1 transport through association with the coding sequence (Ghosh et al., 2012).

Interestingly, when either component of the kinesin-1 transport complex was lacking, basal RNAs were mislocalized to the apical domain in a dynein-dependent process. Therefore, dynein-mediated apical localization represents a "default" mechanism that must be overcome by kinesin-1 to drive basal RNA localization. Two possible scenarios could explain dynein-mediated apical mislocalization upon kinesin inhibition. Dynein and kinesin-1 could be engaged in a tug of war, pulling the RNAs in opposing directions, a phenomenon observed in the transport of vesicles and lipid droplets (Hancock, 2014). Alternatively, the dynein complex could be kept in an inhibited state and activated upon disruption of kinesin-1 and its regulators. If the tug-of-war scenario were correct, we would have expected a change in *zip* RNA localization in all RNAi conditions including *egl* RNAi alone, namely a shift to a more basal localization due to the enhanced Khc-dependent motility. However, since we did not see a significant change in *zip* localization when only Egl was knocked down, the tug-of-war hypothesis appears to be less likely than the inhibition hypothesis. In addition, this phenomenon recalls *osk* RNA mislocalization to the oocyte anterior upon disruption of kinesin-1, *a*Tm1 or EJC components (Brendza et al., 2000; Cha et al., 2002; Erdélyi et al., 1995; Hachet & Ephrussi, 2001; Mohr et al., 2001; Newmark & Boswell, 1994; Palacios et al., 2004; Zimyanin et al., 2008) which was

13

305   hypothesized to occur due to a failure to inactivate dynein-mediated RNA transport (Zimyanin et al.,

306   2008).

307

308   Apical RNA localization, on the other hand, can be divided into two mechanistically distinct categories,

309   both based on dynein-mediated transport. The first category includes those RNAs that are transported

310   apically by the dynein/BicD/Egl machinery, a well characterized RNA transport complex that directs

311   RNAs towards MT minus ends in a variety of tissues (Bullock & Ish-Horowicz, 2001). Our data suggest

312   that the majority of apically localizing RNAs may belong to this class, as the localization of most of our

313   randomly chosen apical RNAs was affected in both *Dhc* RNAi and *egl* RNAi conditions. This

314   hypothesis is consistent with previous studies that identified several apical RNAs as BicD/Egl cargoes,

315   in a variety of *Drosophila* tissues (Li et al., 2008; Bhagavatula & Knust, 2021; Karlin-McGinness et al.,

316   1996; Jambor et al., 2014; Vazquez-Pianzola et al., 2017; Van De Bor et al., 2011).

317

318   The second category of dynein-dependent apical RNAs does not involve Egalitarian activity for their

319   localization. This includes a subgroup of dynein-activating adaptors, namely *BicD, hook,* and *Bsg25D*

320   (*BICD2, HOOK1-3,* and *NIN/NINL* in mammals). Common features of their apical RNA localization

321   include sensitivity to puromycin and partial co-localization with cortical dynein foci containing also *Dhc*

322   RNA. Puromycin causes the disassembly of the translational machinery and the release of the N-

323   terminal peptides emerging from ribosomes. As the N-terminal portion of these adaptors was shown to

324   bind dynein or dynactin subunits (Hoogenraad et al., 2003; Chowdhury et al., 2015; Urnavicius et al.,

325   2015; Schroeder & Vale, 2016; Redwine et al., 2017; Lee et al., 2020), we propose that the apical

326   localization of *BicD, hook,* and *Bsg25D* depends on the co-translational association between dynein

327   components and nascent adaptors at cortical dynein foci (**Figure 6B**). This process might also be

328   conserved in mammals, since the localization of both *BICD2* and *NIN* RNA was shown to be

329   puromycin-sensitive (Safieddine et al., 2021). Previous studies have shown that dynein/dynactin

330   particles have a low affinity to MTs and predominantly exhibit non-processive movements (Torisawa et

331   al., 2014; Trokter et al., 2012). BICD2, HOOK3 and NIN/NINL were shown to promote the formation of

332   highly processive dynein/dynactin complexes (McKenney et al., 2014; Schalager et al., 2014; Redwine

333   et al., 2017). Therefore, it is possible that co-translational assembly of components of the dynein-

334   adaptor complexes is necessary to overcome dynein auto-inhibition (Torisawa et al., 2014; Zhang et

14

335   al., 2017). *BicD, hook,* and *Bsg25D* may co-translationally associate with dynein soon after nuclear

336   export of the RNA, promoting its apical transport in a manner similar to what has been proposed for

337   *PCNT* RNA targeting at centrosomes (Sepulveda et al., 2018). Alternatively, since dynein can also

338   function as a MT-tethered static anchor in mid-oogenesis oocytes and follicle cells (Delanoue & Davis,

339   2005; Delanoue et al., 2007), the interaction between dynein and nascent adaptor proteins could

340   occur after the RNA has reached the cell cortex by dynein-mediated transport. Indeed, puromycin

341   treatment did not completely abolish the apical enrichment of adaptor RNAs, despite causing a

342   marked decrease in their signal close to the apical cortex, where they decorate dynein cortical foci.

343

344   *In vitro* studies have shown that full-length BicD/BICD2 adopts an autoinhibitory conformation resulting

345   from CC1/2 folding onto the CTD-containing CC3 (Hoogenraad et al., 2001; Dienstbier et al., 2009;

346   Stuurman et al., 1999). Although the leading hypothesis in the field is that cargo binding to the CTD is

347   responsible for the alleviation of auto-inhibition by freeing up the N-terminal dynein-binding domain

348   (Dienstbier et al., 2009; Hoogenraad et al., 2001, 2003; Matanis et al., 2002), it is possible that *in vivo*

349   both nascent BicD interaction with dynein and cargo binding to the CTD might cooperate in preventing

350   BicD intramolecular inhibition in the cellular environment. Strikingly, whereas the mechanism

351   underlying oocyte localization of *BicD* RNA during mid-oogenesis resembles that observed in follicle

352   cells, the nurse cell-to-oocyte transport of *BicD* RNA appears to be governed by a different,

353   translation-independent mechanism that may not involve interaction with Dhc/*Dhc* RNA particles,

354   consistent with a previous study indicating that *BicD* RNA is translationally inhibited by Me31B in the

355   nurse cells (Nakamura et al., 2001). In contrast to early egg chambers in which the MT network

356   emanates from a posteriorly-positioned microtubule organizing center in the oocyte, mid-stage oocytes

357   and columnar follicle cells are both characterized by non-centrosomal MTs tethered to the cell cortex

358   (Tillery et al., 2018). Therefore, the establishment of ncMTs could be at the basis of the mechanistic

359   switch from translation-independent to co-translational *BicD* RNA localization in these compartments.

360   Strikingly, a recent report has shown that *NIN* RNA (the mammalian ortholog of *Bsg25D*) localizes at

361   ncMTs and its expression is essential for apico-basal MT formation and columnar epithelial shape

362   (Goldspink et al., 2017). Therefore, it is possible that the co-translational transport of adaptor RNAs

363   may be important for correct ncMT nucleation at the apical cortex of the follicular epithelium.

15

MATERIALS AND METHODS

LCM sample preparation

w1118 virgin females were kept with males for 24 h at 25ºC on yeast-supplemented cornmeal food. Ovaries were dissected in PBS, transferred to a cryomold and snap-frozen in cold 2-Methylbutane after removal of excess PBS. Frozen ovaries were immediately covered with OCT cryoembedding compound (Sakura) and snap-frozen again. Before cryostat sectioning, each block was equilibrated at -20ºC for 1 h. 10 µm cryosections of OCT-embedded ovaries were carefully placed on a MembraneSlide NF 1.0 PEN (Zeiss), briefly thawed at RT and immediately fixed in 75% RNase-free (RF) ethanol for 30 s. Excess OCT was removed with ddH2O RF, and slides were stained in 100 µl Histogene staining solution (Arcturus) according to the manufacturer's instructions. Finally, sections were dehydrated in increasing ethanol concentrations (75%, 95%, 100%), and briefly air-dried before LCM.

LCM and RNA-seq

LCM was performed with a Zeiss PALM MicroBeam and visualized under a 63X objective. Sectioned mid-oogenesis egg chambers were staged according to morphological criteria. Once stage 9-10 egg chambers had been identified, either the apical half ("apical fragment") or the basal half ("basal fragment") of 5-10 contiguous columnar follicle cells was microdissected and collected into the cap of an AdhesiveCap tube (Zeiss). 10 fragments of either apical or basal sample type from different egg chambers were pooled for each replicate, with a total microdissected area of ~3000-4000 μm^2/replicate. LCM samples were processed according to Chen et al. (2017) to produce high-quality Illumina sequencing libraries. Samples were multiplexed and simultaneously sequenced in a single lane using the NextSeq500 system according to the manufacturer's instructions.

RNA-seq analysis

Pre-processing of demultiplexed raw reads was performed on EMBL's instance of Galaxy platform. Read quality was checked after each processing step with FastQC (Andrews, 2010). Low-quality bases and adapter sequences were trimmed from raw read with Trimmomatic (Bolger et al., 2014). rRNA-filtered reads (SortMeRNA, Kopylova et al., 2012) were mapped against *D. melanogaster* Release 6 (dm6) reference genome with STAR (Dobin et al., 2013). To control for RNA degradation

16

394   that might have occurred during LCM, the normalized transcript coverage of the uniquely mapping

395   reads was calculated with CollectRNAseqMetrics (part of Picard tools,

396   http://broadinstitute.github.io/picard/). Uniquely mapped reads were counted with featureCounts (Liao

397   et al., 2014) and normalized with DESeq2 (Love et al., 2014). Differential gene expression analysis

398   was performed with DESeq2 by comparing the mean read counts of the Apical (4 replicates, A1-A4)

399   and Basal (4 replicates, B1-B4) samples. Replicates A5 and B5 were excluded from further analysis

400   due to their high degree of dissimilarity with replicates of the same sample type as shown by PCA and

401   Euclidean distance analysis, probably due to a high degree of contamination from neighboring tissues.

402   Statistical significance was set to an FDR-adjusted p value < 0.1 (Benjamini-Hochberg correction for

403   multiple testing). The R package ComplexHeatmap (Gu et al., 2016) was used to generate the

404   heatmap in Figure 2B.

405

406   **Identification of contaminant reads**

407   Identification of contaminant RNAs was performed with R Studio. Among the RNAs that were

408   significantly enriched in either the apical (log2FC > 0) or the basal (log2FC < 0) domain, were

409   considered "contaminants" those RNAs displaying high absolute log2FoldChange (|log2FC|),

410   indicating that they were probably originating from neighboring tissues. A threshold of log2FC > 3 and

411   log2FC < -3 was arbitrarily set to identify putative apical and basal contaminants, respectively. The

412   functional annotation of each contaminant candidate was retrieved on FlyBase (release FB2020_6)

413   (Larkin et al., 2021) and their read distribution among apical and basal replicates analyzed through

414   Integrative Genomics Viewer (IGV) (Robinson et al., 2011).

415

416   **Fly stocks and genetics**

417   All fly stocks were maintained at 18°C on standard fly food. For crosses, virgin females were mated

418   with *w1118* males at 25°C on cornmeal food supplemented with yeast. Female offspring of the desired

419   genotype were incubated with *w1118* males on a yeast-supplemented medium for 24h at 25°C to

420   stimulate the development of vitellogenic stage egg-chambers before ovary dissection.

421   The following stocks were obtained from the Bloomington Drosophila Stock Center (BDSC): *w1118*

422   (wild-type; #3605), *DhcRNAi* (#36698), *eglRNAi* (#28969), *KhcRNAi* (#35409), *UAS-NLS-mCherry*

423   (#38425), *osk-Gal4* (#44242), *VK33* (#9750). Other stocks used were: *HsFLP; arm>f+>Gal4;*

17

424   *UAS-CD8-mCherry* and *tj-Gal4/CyO* (gifts of Juan Manuel Gomez Elliff), *Tm1eg1/TM3Sb,Ser* and

425   *Tm1eg9/TM3Sb,Ser* (Erdélyi et al., 1995), *Dhc64C-GFP* (Gáspár et al., 2021), *vasa-Gal4/TM3Sb* (gift

426   of Jean Rene Huynh), *UAS-ΔC-Pym-GFP* (Ghosh et al., 2014), *UAS-Egl* (Bullock et al., 2006),

427   *eglWU50/SM1* and *eglPR29/SM6A* (Mach & Lehmann, 1997). Transgenic flies carrying *UAS-GFP*, *UAS-*

428   *0BicD-GFP*, *UAS-(+1)BicD-GFP*, and *UAS-(-1)BicD-GFP* were generated in this study by phiC31

429   integrase-mediated recombination using the VK33 line, which carries an attP site on the third

430   chromosome.

431   For the generation of *eglNULLFC* flies, *eglWU50/CyO*; *osk-Gal4/TM3Ser* were crossed with *eglPR29/CyO*;

432   *UAS-Egl/TM3Ser* to generate *eglWU50/eglPR29*; *osk-Gal4/UAS-Egl*, expressing Egl only in the germline

433   lineage to rescue the formation of rudimentary ovaries. *tj-Gal4* and *vasa-Gal4* drivers were used to

434   express UAS-containing transgenes in the whole follicular epithelium and in the germline, respectively.

435   To generate flies for FC mutant clone induction, male flies carrying a UAS-containing transgene were

436   crossed with *hsFlp; arm>f+>Gal4; UAS-CD8-mCherry* virgins, and F1 females were subjected to heat-

437   shock as described below.

438   To generate flies for induction of FC mutant clones in the experiment illustrated in Figure S3, *HsFLP;*

439   *arm>f+>Gal4/CyO; KhcRNAi/TM6B,Tb* flies were crossed with *+; UAS-NLS-mCherry/CyO;*

440   *eglRNAi/TM3Ser*. F1 Female flies the desired genotypes [*eglRNAi/TM6B,Tb* for the *egl* RNAi

441   condition; *KhcRNAi/TM3Ser* for the *Khc* RNAi condition; *eglRNAi/KhcRNAi* for the (*egl+Khc)* RNAi

442   condition] were collected and subjected to heat-shock as described below.

443

444   **Generation of follicle cell clones**

445   The UAS-Gal4 "flip-out" system was used to generate marked mutant clones in a wild-type

446   background (Struhl & Basler, 1983; Pignoni & Zipurski, 1997). Freshly eclosed females resulting from

447   each cross were collected and mated with *w1118* males for 24 h at 25°C on food supplemented with

448   yeast. Flies were heat-shocked for 1h in a water bath heated at 37°C. According to Gonzales-Reyes &

449   St Johnston (1998), heat-shocked females were kept for 39 h at 25°C with males on yeast before

450   dissection, thus allowing follicle cells that induced the expression of the transgene at stage ~ 5 to

451   develop into stage 10 follicle cells.

452

453   *Ex vivo* **pharmacological treatment**

18

454   Young *w1118* female flies were incubated with males for 24 h at 25°C on fly food supplemented with

455   yeast. Ovaries were dissected in PBS and immediately incubated in Schneider's medium (Gibco)

456   supplemented with 15% FBS (Gibco), 0.6X penicillin/streptomycin (Invitrogen), 200 µg/ml insulin

457   (Sigma). For translation inhibitor treatment, either 200 µg/ml puromycin (Gibco) or 200 µg/ml

458   cycloheximide (Sigma) or no compound (control) was added fresh to the medium and ovaries were

459   incubated for 30 min at RT before fixation.

460

461   **Generation of BicD-GFP constructs and transgenic fly lines**

462   AttB-pUASp-BicD-GFP-K10 or AttB-pUASp-GFP-K10 plasmids carrying a *w+* cassette, a TLS-

463   deficient version of the K10 3'UTR, and attB sites for phiC31 integrase-mediated recombination into

464   the VK33 line were generated as follows.

465   To generate plasmid vectors carrying the BicD-GFP gene cassettes (^{0}*BicD-GFP*, $^{(-1)}$*BicD-GFP*,

466    $^{(+1)}$*BicD-GFP*, *GFP*), BicD and GFP CDS were amplified by PCR and the two fragments were

467   combined into AttB-pUASp-K10 vector by InFusion cloning (Clontech) according to the manufacturer's

468   instructions. pBS-BicD (BicD-RA, FlyBase ID: FBpp0080555) plasmid (a kind gift from Jean-Baptiste

469   Coutelis) was used as template to generate BicD CDS PCR amplicons. The Fw primer used to amplify

470   BicD CDS was designed in order to include, in addition to a 20 nt-homology with AttB-pUASp-K10

471   vector, the *Drosophila* Kozak sequence (Cavener, 1987) in frame with a linker sequence where

472   frameshift mutations could be generated, and a region annealing to nt 4-29 of BicD CDS. To generate

473   ^{0}*BicD-GFP* construct, the 18-bp linker containing the ATG (5'- <u>ATG</u>ATCCTAGGCGCGCGG- 3') was

474   inserted in frame with nt 4-2346 of BicD-RA. To generate $^{(+1)}$*BicD-GFP* construct, a C was inserted at

475   position 4 in the N-terminal 18-bp linker (5'- ATG**C**ATCCTAGGCGCGCGG- 3'). To generate $^{(-1)}$*BicD-*

476   *GFP* construct, a G was deleted at position 10 in the N-terminal 18-bp linker (5'-

477   ATGATCCTA_GCGCGCGG- 3'). ^{0}*BicD-GFP*, $^{(-1)}$*BicD-GFP*, and $^{(+1)}$*BicD-GFP* full insert sequences

478   with the respective predicted translated ORF are listed in **File S2**.

479   To generate UAS-GFP construct, GFP ORF was amplified with a Fw primer containing KpnI restriction

480   site upstream of GFP ATG and with a Rev primer containing NotI restriction site and the stop codon.

481   The amplified fragment was gel purified, digested with KpnI and NotI and ligated into a AttB-pUASp-

482   K10 vector digested with the same enzymes.

483 Each AttB-containing plasmid was purified and sequenced before injection into VK33 embryos

484 carrying an attP site on the 3rd chromosome. Injected flies were crossed with *If/CyO; Sb/TM3Ser*

485 individuals and transgenic F1 flies were identified by appearance of red eye color.

486

487 **Immunostaining**

488 5-10 pairs of ovaries were dissected in PBS and immediately fixed in 2% PFA in PBSTX(0.1%) (PBS

489 + 0.1% Triton-X100) on a Nutator for 20 min at RT, followed by two washes of 15 min each with

490 PBSTX(0.1%) shaking at RT. Ovaries were then blocked in 1X casein/PBSTX(0.1%) (stock: 10X

491 casein blocking buffer, Sigma) for 30 min and incubated with rabbit anti-Egl primary antibody (kind gift

492 from R. Lehmann, Mach & Lehmann, 1997) diluted in blocking buffer o/n at 4°C. Alexa fluor 647 goat

493 anti Rabbit (Jackson Immuno Research) secondary antibody was added in blocking buffer for 2 h at

494 RT. Samples were washed 3x 10 min with 1X casein/PBSTX(0.1%), 1x 10 min with PBSTX(0.1%) +

495 1:15,000 DAPI and kept o/n in 100 µl of 80% TDE/PBS before mounting on microscope slides.

496

497 **Single molecule *in situ* Fluorescence Hybridization (smFISH)**

498 smFISH antisense oligonucleotides (listed in **Table S2**) were designed and labelled with dye-

499 conjugated ddUTPs according to the protocol described by Gáspár et al. (2017) to generate

500 oligonucleotides labelled at their 3' and with ATTO-633-NHS ester (ATTO-TEC). When dual-color

501 smFISH experiments were performed, each probe set was labelled with either ATTO-633 or ATTO-

502 565. The degree of labelling (DOL, % of labelled oligos) and concentration of the labelled probe sets

503 was measured according to the published algorithm.

504 Dissected ovaries were immediately fixed in 2% PFA/PBSTX(0.1%) gently shaking for 20 min at RT.

505 In case of *ex vivo* ovary incubation, dissected ovaries were incubated in Schneider's medium

506 supplemented with the respective pharmacological treatment before proceeding with fixation, as

507 described above. Fixed ovaries were rinsed and washed twice with PBSTX(0.1%) for 10 min before

508 dehydrating them by replacing PBSTX(0.1%) with increasing concentrations of ethanol/PBSTX(0.1%).

509 Fixed and dehydrated ovaries were kept in 100% ethanol at -20°C for up to 10 days until the day of

510 the experiment.

511 An optimized version of the smFISH protocol described in Hampoelz et al. (2019) was followed with

512 minor modifications. All steps were performed at RT unless specified otherwise. Dehydrated ovaries

20

513   were first rinsed with PBSTX(0.1%), followed by 2x15 min washes with PBSTX(0.1%), and incubated

514   in Pre-hybridization Buffer (2x SSC, 10% deionized formamide, 0.1% Tween-20) gently shaking for 30

515   min. The Pre-hybridization Buffer was replaced with 250 µl of Hybridization Buffer (2x SSC, 10%

516   deionized formamide, 0.1% Tween-20, 2 mM vanadyl ribonucleoside complex (New England Biolabs),

517   100 µg/mL salmon sperm DNA (Invitrogen), 10% dextran sulfate, 20 µg/mL BSA) pre-warmed at 37°C

518   in which smFISH probes were added to a final concentration of 1 nM/probe. Ovaries were kept

519   hybridizing in the dark for 16-17 h on a heat block set at 37°C shaking at 1000 rpm. To remove the

520   excess probes, ovaries where washed 3x 10 min at 37°C with Washing Buffer (2x SSC, 10%

521   deionized formamide, 0.1% Tween-20). 1:15,000 DAPI was added to the second wash. Finally,

522   samples were rinsed 4x in PBST(0.1%) (PBS + 0.1% Tween20) and kept in in 100 µl of 80%

523   TDE/PBS for at least 1 h before mounting on microscope slides.

524   Z-stacks of images were acquired on a Leica TCS SP8 confocal microscope with 405nm, 488 nm, 552

525   nm and 640 nm fixed excitation laser lines using a 63X 1.3 NA glycerol immersion objective. A suitable

526   range for spectral detection was carefully chosen for each channel to avoid cross-talk of fluorescence

527   emission. Images were automatically restored by deconvolution with the Lightning module.

528

529   **Image analysis and statistical testing**

530   To quantify smFISH fluorescence of localizing RNAs, average Z-projections of deconvolved confocal

531   image stacks were analyzed with Fiji (Schindelin et al., 2012). In mosaic FE, for each wild-type (wt,

532   unmarked) and mutant (mCherry-marked) group of cells within the same Z-stack, a region of interest

533   (ROI) was drawn encompassing the apical and the basal cytoplasm of 5-10 adjacent follicle cells (with

534   the exclusion of nuclei); in addition, a ROI was drawn in an area of the image were no signal was

535   present (background, bg). The mean fluorescence intensity (m.f.i.) was measured for each ROI.

536   The degree of apicality (DoA) of a given RNA in each cell type (*t*) (wild-type or mutant) and each

537   experimental condition *c*, was measured as follows:

538    $$DoA_{t,c} = \left(\frac{Apical\ m.f.i_t - bg\ m.f.i}{Basal\ m.f.i_t - bg\ m.f.i}\right)_c$$

539   To quantitatively analyze changes in RNA localization in each experimental condition *c*, the DoA

540   measured in mutant (KD) cells was divided by the DoA measured in neighboring wild-type (wt) cells

541   within the same Z-stack:

21

542
$$KD/wt\,DoA_c = \left(\frac{DoA_{KD}}{DoA_{wt}}\right)_c$$

543 Only in $Tm1^{NULL}$ condition, due to the impossibility to obtain a mosaic tissue, the DoA of a given RNA

544 in each cell type (t) (wild-type or $Tm1^{NULL}$), was measured as follows:

545
$$DoA_t = \left(\frac{Apical\,m.f.i\ -bg\,m.f.i}{Basal\,m.f.i\ -bg\,m.f.i}\right)_t$$

546 To calculate the change in DoA, the DoA measured in single $Tm1^{NULL}$ egg chambers was divided by

547 the average DoA measured in n wild-type egg chambers (wt):

548
$$Tm1NULL/wt\,DoA = \frac{DoA_{Tm1NULL}}{\frac{1}{n}\sum DoA_{wt}}$$

549 In Figure 2D, Figure 3C, and Figure 5D, KD/wt DoA values of each RNA and experimental condition

550 was measured across at least 3 different Z-projections, and the average value obtained was

551 compared to the null hypothesis H_0: KD/wt DoA=1, corresponding to no change in RNA localization

552 bias following KD treatment [DoA(KD)=DoA(wt)]. One-sample Student's t-test was used to compare

553 means to a reference value of mu = 1 in each experimental condition.

554 In Figure S3B, independent Student's t-test was used to compare mean DoA(wt) and DoA(RNAi)

555 values in each condition. In Figure S3C, mean KD/wt DoA values across conditions were compared by

556 one-way ANOVA followed by Tukey's post-hoc tests.

557

558 **Other image analysis and statistical procedures**

559 Fluorescence intensity along lines were measured with Fiji on average Z-projections of confocal

560 images and plotted with R Studio. Intensity values from each channel were normalized to 0-1 range.

561 *BicD, GFP, Bsg25D or hook* mean fluorescence intensity along the A-B axis of the epithelium was

562 measured in groups of 5-10 adjacent follicle cells as line plots. At least 3 line plots were generated for

563 each RNA measured in each condition. The value corresponding to 50% of the cumulative area under

564 the curve (a.u.c.) of each plot was considered as the variation of the respective RNA localization along

565 the A-B axis of the epithelium. Welch two sample t-test was used to compare mean values of the 50%

566 of the a.u.c with respect to untreated controls (pharmacological experiments) or in-frame *BicD-GFP*

567 (*Frameshift* vs. *In-frame* variation).

568

569 **DATA AVAILABILITY**

570 The authors declare that all data supporting the findings of this study are available within the article

571 and its supplementary information files or from the corresponding author upon reasonable request.

572 RNA-seq data have been deposited in the ArrayExpress database at EMBL-EBI

573 (www.ebi.ac.uk/arrayexpress) under accession number E-MTAB-9127.

574

575 **AUTHOR CONTRIBUTIONS**

576 Conceptualization, L.C. and A.E.; Investigation, L.C.; Data Analysis, L.C; Writing – Original Draft, L.C.;

577 Writing – Review & Editing, L.C. and A.E; Supervision, A.E.; Funding Acquisition, A.E.

578

579 **ACKNOWLEDGEMENTS**

590

591 **DECLARATION OF INTERESTS**

592 The authors declare no competing financial interests.

593

594 **REFERENCES**

595 Andrews S (2010). A Quality Control Tool for High Throughput Sequence Data [Online]. Available
596   online at: http://www.bioinformatics.babraham.ac.uk/projects/fastqc/

597 Baumann S, König J, Koepke J, Feldbrügge M (2014) Endosomal transport of septin mRNA and
598   protein indicates local translation on endosomes and is required for correct septin filamentation.
599   *EMBO Rep* 15: 94–102

600 Bhagavatula S, Knust E (2021) A putative stem-loop structure in Drosophila crumbs is required for
601   mRNA localisation in epithelia and germline cells. *J Cell Sci* 134

602 Blower MD, Feric E, Weis K, Heald R (2007) Genome-wide analysis demonstrates conserved
603   localization of messenger RNAs to mitotic microtubules. *J Cell Biol* 179: 1365–1373

604 Bolger AM, Lohse M, Usadel B (2014) Trimmomatic: A flexible trimmer for Illumina sequence data.
605   *Bioinformatics* 30: 2114–2120

606 Brendza RP, Serbus LR, Duffy JB, Saxton WM, Brendza RP, Serbus LR, Duffy JB, Saxton WM (2000)
607   A Function for Kinesin I in the Posterior Transport of oskar mRNA and Staufen Protein. *Science*
608   *(80-)* 289: 2120–2122

609 Bullock SL, Nicol A, Gross SP, Zicha D (2006) Guidance of Bidirectional Motor Complexes by mRNA
610   Cargoes through Control of Dynein Number and Activity. *Curr Biol* 16: 1447–1452

611 Bullock SL, Ish-Horowicz D (2001) Conserved signals and machinery for RNA transport in Drosophila
612   oogenesis and embryogenesis. *Nature* 414: 611–616

613 Cavener DR (1987) Comparison of the consensus sequence flanking translational start sites in
614   Drosophila and vertebrates. *Nucleic Acids Res* 15: 1353–1361

615 Cha B-J, Serbus LR, Koppetsch BS, Theurkauf WE (2002) Kinesin I-dependent cortical exclusion
616   restricts pole plasm to the oocyte posterior. *Nat Cell Biol* 4: 592–598

617 Chen J, Suo S, Tam PP, Han JDJ, Peng G, Jing N (2017) Spatial transcriptomic analysis of
618   cryosectioned tissue samples with Geo-seq. *Nat Protoc* 12: 566–580

619 Chowdhury S, Ketcham SA, Schroer TA, Lander GC (2015) Structural organization of the dynein-
620   dynactin complex bound to microtubules. *Nat Struct Mol Biol* 22: 345–347

621 Cioni JM, Lin JQ, Holtermann A V., Koppers M, Jakobs MAH, Azizi A, Turner-Bridger B, Shigeoka T,
622   Franze K, Harris WA, *et al* (2019) Late Endosomes Act as mRNA Translation Platforms and
623   Sustain Mitochondria in Axons. *Cell* 176: 56–72

624 Clark A, Meignin C, Davis I (2007) A Dynein-dependent shortcut rapidly delivers axis determination
625   transcripts into the Drosophila oocyte. *Development* 134: 1955–1965

626 Clark IE, Jan LY, Jan YN (1997) Reciprocal localization of nod and kinesin fusion proteins indicates
627   microtubule polarity in the Drosophila oocyte, epithelium, neuron and muscle. *Development* 124:
628   461–470

629 Cohen B, Golani-Armon A, Altman T, Savulescu AF, Mhlanga MM, Perlson E, Arava YS (2021)
630   Mitochondria serve as axonal shuttle for Cox7c mRNA through mechanism that involves its
631   mitochondrial targeting signal. *bioRxiv*: 2021.05.19.444640

632 Corradi E, Dalla Costa I, Gavoci A, Iyer A, Roccuzzo M, Otto TA, Oliani E, Bridi S, Strohbuecker S,
633   Santos-Rodriguez G, *et al* (2020) Axonal precursor miRNAs hitchhike on endosomes and locally
634   regulate the development of neural circuits. *EMBO J* 39: 1–24

635 Coutelis JB, Ephrussi A (2007) Rab6 mediates membrane organization and determinant localization
636   during Drosophila oogenesis. *Development* 134: 1419–1430

637 Delanoue R, Davis I (2005) Dynein anchors its mRNA cargo after apical transport in the Drosophila
638   blastoderm embryo. *Cell* 122: 97–106

24

639 Delanoue R, Herpers B, Soetaert J, Davis I, Rabouille C (2007) Drosophila Squid/hnRNP Helps
640   Dynein Switch from a gurken mRNA Transport Motor to an Ultrastructural Static Anchor in
641   Sponge Bodies. *Dev Cell* 13: 523–538

642 Dienstbier M, Boehl F, Li X, Bullock SL (2009) Egalitarian is a selective RNA-binding protein linking
643   mRNA localization signals to the dynein motor. *Genes Dev* 23: 1546–1558

644 Dimitrova-Paternoga L, Jagtap PKA, Cyrklaff A, Vaishali, Lapouge K, Sehr P, Perez K, Heber S, Löw
645   C, Hennig J, *et al* (2021) Molecular basis of mRNA transport by a kinesin-1-atypical tropomyosin
646   complex. *Genes Dev* 35: 1–16

647 Dobin A, Davis CA, Schlesinger F, Drenkow J, Zaleski C, Jha S, Batut P, Chaisson M, Gingeras TR
648   (2013) STAR: Ultrafast universal RNA-seq aligner. *Bioinformatics* 29: 15–21

649 Erdélyi M, Michon AM, Guichet A, Glotzer JB, Ephrussi A (1995) Requirement for Drosophila
650   cytoplasmic tropomyosin in oskar mRNA localization. *Nature* 377: 524–527

651 Gardiol A, St Johnston D (2014) Staufen targets coracle mRNA to Drosophila neuromuscular junctions
652   and regulates GluRIIA synaptic accumulation and bouton number. *Dev Biol* 392: 153–167

653 Gáspár I, Phea LJ, Ephrussi A (2021) Egalitarian feeds forward to Staufen to inhibit Dynein during
654   mRNP transport. *bioRxiv*: 2021.04.24.441269

655 Gáspár I, Sysoev V, Komissarov A, Ephrussi A (2016) An RNA-binding atypical tropomyosin recruits
656   kinesin-1 dynamically to oskar mRNPs. *EMBO J* 36: 319–333

657 Gáspár I, Wippich F, Ephrussi A (2017) Enzymatic production of single-molecule FISH and RNA
658   capture probes. *Rna* 23: 1582–1591

659 Ghosh S, Obrdlik A, Marchand V, Ephrussi A (2014) The EJC Binding and Dissociating Activity of
660   PYM Is Regulated in Drosophila. *PLoS Genet* 10: e1004455

661 Goldspink DA, Rookyard C, Tyrrell BJ, Gadsby J, Perkins J, Lund EK, Galjart N, Thomas P, Wileman
662   T, Mogensen MM (2017) Ninein is essential for apico-basal microtubule formation and CLIP-170
663   facilitates its redeployment to non-centrosomal microtubule organizing centres. *Open Biol* 7

664 González-Reyes A, St Johnston D (1998) Patterning and morphogenesis of the follicle cell epithelium
665   during Drosophila oogenesis. *Development* 125: 2837–2846

666 Gu Z, Eils R & Schlesner M (2016) Complex heatmaps reveal patterns and correlations in
667   multidimensional genomic data. *Bioinformatics* 32: 2847–2849

668 Hachet O, Ephrussi A (2001) Drosophila Y14 shuttles to the posterior of the oocyte and is required for
669   oskar mRNA transport. *Curr Biol* 11: 1666–1674

670 Hampoelz B, Schwarz A, Ronchi P, Bragulat-Teixidor H, Tischer C, Gaspar I, Ephrussi A, Schwab Y,
671   Beck M (2019) Nuclear Pores Assemble from Nucleoporin Condensates During Oogenesis. *Cell*
672   179: 671-686.e17

673 Hancock WO (2014) Bidirectional cargo transport: Moving beyond tug of war. *Nat Rev Mol Cell Biol*
674   15: 615–628

675 Harbauer AB, Wanderoy S, Hees JT, Gibbs W, Ordonez M, Cai Z, Cartoni R, Ashrafi G, Wang C, He
676   Z, *et al* (2021) Neuronal mitochondria transport Pink1 mRNA via Synaptojanin 2 to support local
677   mitophagy. *bioRxiv*: 2021.05.19.444778

678   Hoogenraad CC, Akhmanova A, Howell SA, Dortland BR, De Zeeuw CI, Willemsen R, Visser P,
679   Grosveld F, Galjart N (2001) Mammalian golgi-associated Bicaudal-D2 functions in the dynein-
680   dynactin pathway by interacting with these complexes. *EMBO J* 20: 4041–4054

681   Hoogenraad CC, Wulf P, Schiefermeier N, Stepanova T, Galjart N, Small JV, Grosveld F, De Zeeuw
682   CI, Akhmanova A (2003) Bicaudal D induces selective dynein-mediated microtubule minus end-
683   directed transport. *EMBO J* 22: 6004–6015

684   Horne-Badovinac S, Bilder D (2008) Dynein regulates epithelial polarity and the apical localization of
685   stardust A mRNA. *PLoS Genet* 4: 0040–0051

686   Hughes JR, Bullock SL, Ish-Horowicz D (2004) inscuteable mRNA Localization Is Dynein-Dependent
687   and Regulates Apicobasal Polarity and Spindle Length in Drosophila Neuroblasts. *Curr Biol* 14:
688   1950–1956

689   Jambor H, Mueller S, Bullock SL, Ephrussi A (2014) A stem-loop structure directs oskar mRNA to
690   microtubule minus ends. *Rna* 20: 429–439

691   Jambor H, Surendranath V, Kalinka AT, Mejstrik P, Saalfeld S, Tomancak P (2015) Systematic
692   imaging reveals features and changing localization of mRNAs in Drosophila development. *Elife*
693   4: 1–22

694   Januschke J, Nicolas E, Compagnon J, Formstecher E, Goud B, Guichet A (2007) Rab6 and the
695   secretory pathway affect oocyte polarity in Drosophila. *Development* 134: 3419–3425

696   Karlin-McGinness M, Serano TL, Cohen RS (1996) Comparative Analysis of the Kinetics and
697   Dynamics of K10, bicoid, and oskar mRNA Localization in the Drosophila Oocyte. *Dev Genet* 19:
698   238–248

699   Khanal I, Elbediwy A, de la Loza M del CD, Fletcher GC, Thompson BJ (2016) Shot and Patronin
700   polarise microtubules to direct membrane traffic and biogenesis of microvilli in epithelia. *J Cell*
701   *Sci* 129: 2651–2659

702   Kopylova E, Noé L, Touzet H (2012) SortMeRNA: Fast and accurate filtering of ribosomal RNAs in
703   metatranscriptomic data. *Bioinformatics* 28: 3211–3217

704   Kwon OS, Mishra R, Safieddine A, Coleno E, Alasseur Q, Faucourt M, Barbosa I, Bertrand E, Spassky
705   N, Le Hir H (2021) Exon junction complex dependent mRNA localization is linked to centrosome
706   organization during ciliogenesis. *Nat Commun* 12: 1–16

707   Larkin A, Marygold SJ, Antonazzo G, Attrill H, dos Santos G, Garapati P V, Goodman JL, Gramates
708   LS, Millburn G, Strelets VB, *et al* (2021) FlyBase: updates to the Drosophila melanogaster
709   knowledge base. *Nucleic Acids Res* 49: D899–D907

710   Lécuyer E, Yoshida H, Parthasarathy N, Alm C, Babak T, Cerovina T, Hughes TR, Tomancak P,
711   Krause HM (2007) Global Analysis of mRNA Localization Reveals a Prominent Role in
712   Organizing Cellular Architecture and Function. *Cell* 131: 174–187

713   Lee I-G, Cason SE, Alqassim SS, Holzbaur ELF, Dominguez R (2020) A tunable LIC1-adaptor
714   interaction modulates dynein activity in a cargo-specific manner. *Nat Commun* 11: 5695

715   Li Z, Wang L, Hays TS, Cai Y (2008) Dynein-mediated apical localization of crumbs transcripts is
716   required for Crumbs activity in epithelial polarity. *J Cell Biol* 180: 31–38

717   Liao YC, Fernandopulle MS, Wang G, Choi H, Hao L, Drerup CM, Patel R, Qamar S, Nixon-Abell J,
718   Shen Y, *et al* (2019) RNA Granules Hitchhike on Lysosomes for Long-Distance Transport, Using
719   Annexin A11 as a Molecular Tether. *Cell* 179: 147–164

720 Liao Y, Smyth GK, Shi W (2014) FeatureCounts: An efficient general purpose program for assigning
721   sequence reads to genomic features. *Bioinformatics* 30: 923–930

722 Love MI, Huber W, Anders S (2014) Moderated estimation of fold change and dispersion for RNA-seq
723   data with DESeq2. *Genome Biol* 15: 1–21

724 Mach JM, Lehmann R (1997) An Egalitarian-BicaudalD Complex Is Essential for Oocyte Specification
725   and Axis Determination in Drosophila. *Genes Dev* 11: 423–435

726 Matanis T, Akhmanova A, Wulf P, Del Nery E, Weide T, Stepanova T, Galjart N, Grosveld F, Goud B,
727   De Zeeuw CI, *et al* (2002) Bicaudal-D regulates COPI-independent Golgi-ER transport by
728   recruiting the dynein-dynactin motor complex. *Nat Cell Biol* 4: 986–992

729 McKenney RJ, Huynh W, Tanenbaum ME, Bhabha G, Vale RD (2014) Activation of cytoplasmic
730   dynein motility by dynactin-cargo adapter complexes. *Science (80-)* 345: 337–341

731 Medioni C, Mowry K, Besse F (2012) Principles and roles of mRNA localization in animal
732   development. *Development* 139: 3263–3276

733 Mili S, Moissoglu K, Macara IG (2008) Genome-wide screen reveals APC-associated RNAs enriched
734   in cell protrusions. *Nature* 453: 115–119

735 Mohr SE, Dillon ST, Boswell RE (2001) The RNA-binding protein Tsunagi interacts with Mago Nashi to
736   establish polarity and localize oskar mRNA during Drosophila oogenesis. *Genes Dev* 15: 2886–
737   2899

738 Moor AE, Golan M, Massasa EE, Lemze D, Weizman T, Shenhav R, Baydatch S, Mizrahi O, Winkler
739   R, Golani O, *et al* (2017) Global mRNA polarization regulates translation efficiency in the
740   intestinal epithelium. *Science (80-)* 357: 1299–1303

741 Nakamura A, Amikura R, Hanyu K, Kobayashi S (2001) Me31B silences translation of oocyte-
742   localizing RNAs through the formation of cytoplasmic RNP complex during Drosophila
743   oogenesis. *Development* 128: 3233–3242

744 Navarro C, Puthalakath H, Adams JM, Strasser A, Lehmann R (2004) Egalitarian binds dynein light
745   chain to establish oocyte polarity and maintain oocyte fate. *Nat Cell Biol* 6: 427–435

746 Newmark PA, Boswell RE (1994) The mago nashi locus encodes an essential product required for
747   germ plasm assembly in Drosophila. *Development* 120: 1303–1313

748 Olenick MA, Holzbaur ELF (2019) Dynein activators and adaptors at a glance. *J Cell Sci* 132

749 Palacios IM, Gatfield D, St. Johnston D, Izaurralde E (2004) An eIF4AIII-containing complex required
750   for mRNA localization and nonsense-mediated mRNA decay. *Nature* 427: 753–757

751 Pignoni F, Zipursky SL (1997) Induction of Drosophila eye development by decapentaplegic.
752   *Development* 124: 271–278

753 Redwine WB, DeSantis ME, Hollyer I, Htet ZM, Tran PT, Swanson SK, Florens L, Washburn MP,
754   Reck-Peterson SL (2017) The human cytoplasmic dynein interactome reveals novel activators of
755   motility. *Elife* 6: 1–27

756 Robinson J, Thorvaldsdóttir H, Winckler W, Guttman M, Lander ES, Getz G, Mesirov JP (2011)
757   Integrative genomics viewer. *Nat Biotechnol* 29: 24–26 doi:10.1038/nbt.1754

758 Ronchi P, Mizzon G, Machado P, D'Imprima E, Best BT, Cassella L, Schnorrenberg S, Montero MG,
759   Jechlinger M, Ephrussi A, *et al* (2021) High-precision targeting workflow for volume electron
760   microscopy. *J Cell Biol* 220

761 Safieddine A, Coleno E, Salloum S, Imbert A, Traboulsi AM, Kwon OS, Lionneton F, Georget V,
762   Robert MC, Gostan T, *et al* (2021) A choreography of centrosomal mRNAs reveals a conserved
763   localization mechanism involving active polysome transport. *Nat Commun* 12: 1–21

764 Schindelin J, Arganda-Carreras I, Frise E, Kaynig V, Longair M, Pietzsch T, Preibisch S, Rueden C,
765   Saalfeld S, Schmid B, *et al* (2012) Fiji: An open-source platform for biological-image analysis.
766   *Nat Methods* 9: 676–682

767 Schlager MA, Serra-Marques A, Grigoriev I, Gumy LF, da Silva ME, Wulf PS, Akhmanova A,
768   Hoogenraad CC (2014) Bicaudal D Family Adaptor Proteins Control the Velocity of Dynein-
769   Based Movements. *Cell Rep* 8: 1248–1256

770 Schotman H, Karhinen L, Rabouille C (2008) dGRASP-Mediated Noncanonical Integrin Secretion Is
771   Required for Drosophila Epithelial Remodeling. *Dev Cell* 14: 171–182

772 Schroeder CM, Vale RD (2016) Assembly and activation of dynein-dynactin by the cargo adaptor
773   protein Hook3. *J Cell Biol* 214: 309–318

774 Sepulveda G, Antkowiak M, Brust-Mascher I, Mahe K, Ou T, Castro NM, Christensen LN, Cheung L,
775   Jiang X, Yoon D, *et al* (2018) Co-translational protein targeting facilitates centrosomal
776   recruitment of PCNT during centrosome maturation in vertebrates. *Elife* 7: 1–28

777 Serano J, Rubin GM (2003) The Drosophila synaptotagmin-like protein bitesize is required for growth
778   and has mRNA localization sequences within its open reading frame. *Proc Natl Acad Sci U S A*
779   100: 13368–13373

780 Shepard KA, Gerber AP, Jambhekar A, Takizawa PA, Brown PO, Herschlag D, DeRisi JL, Vale RD
781   (2003) Widespread cytoplasmic mRNA transport in yeast: Identification of 22 bud-localized
782   transcripts using DNA microarray analysis. *Proc Natl Acad Sci U S A* 100: 11429–11434

783 Sladewski TE, Billington N, Ali MY, Bookwalter CS, Lu H, Krementsova EB, Schroer TA, Trybus KM
784   (2018) Recruitment of two dyneins to an mRNA-dependent bicaudal D transport complex. *Elife* 7:
785   e36306

786 Steinhauer J, Kalderon D (2006) Microtubule polarity and axis formation in the Drosophila oocyte. *Dev
787   Dyn an Off Publ Am Assoc Anat* 235: 1455–1468

788 Struhl G, Basler K (1993) Organizing activity of wingless protein in Drosophila. *Cell* 72: 527–540

789 Stuurman N, Häner M, Sasse B, Hübner W, Suter B, Aebi U (1999) Interactions between coiled-coil
790   proteins: Drosophila lamin Dm0 binds to the Bicaudal-D protein. *Eur J Cell Biol* 78: 278–287

791 Suter B, Steward R (1991) Requirement for phosphorylation and localization of the Bicaudal-D protein
792   in Drosophila oocyte differentiation. *Cell* 67: 917–926

793 Tillery MML, Blake-Hedges C, Zheng Y, Buchwalter RA, Megraw TL (2018) Centrosomal and Non-
794   Centrosomal Microtubule-Organizing Centers (MTOCs) in Drosophila melanogaster. *Cells* 7: 121

795 Torisawa T, Ichikawa M, Furuta A, Saito K, Oiwa K, Kojima H, Toyoshima YY, Furuta K (2014)
796   Autoinhibition and cooperative activation mechanisms of cytoplasmic dynein. *Nat Cell Biol* 16:
797   1118–1124

798   Trokter M, Mücke N, Surrey T (2012) Reconstitution of the human cytoplasmic dynein complex. *Proc*
799   *Natl Acad Sci* 109: 20895 LP – 20900

800   Urnavicius L, Zhang K, Diamant AG, Motz C, Schlager MA, Yu M, Patel NA, Robinson C V, Carter AP
801   (2015) The structure of the dynactin complex and its interaction with dynein. *Science* 347: 1441–
802   1446

803   Van de Bor V, Zimniak G, Cérézo D, Schaub S, Noselli S (2011) Asymmetric localisation of cytokine
804   mRNA is essential for JAK/STAT activation during cell invasiveness. *Development* 138: 1383–
805   1393

806   Vazquez-Pianzola P, Schaller B, Colombo M, Beuchle D, Neuenschwander S, Marcil A, Bruggmann
807   R, Suter B (2017) The mRNA transportome of the BicD/Egl transport machinery. *RNA Biol* 14:
808   73–89

809   Wharton RP, Struhl G (1989) Structure of the Drosophila BicaudalD protein and its role in localizing
810   the posterior determinant nanos. *Cell* 59: 881–892

811   Wilk R, Hu J, Blotsky D, Krause HM (2016) Diverse and pervasive subcellular distributions for both
812   coding and long noncoding RNAs. *Genes Dev* 30: 594–609

813   Wilkie GS, Davis I (2001) Drosophila wingless and pair-rule transcripts localize apically by dynein-
814   mediated transport of RNA particles. *Cell* 105: 209–219

815   Xing L, Bassell GJ (2013) MRNA localization: An orchestration of assembly, traffic and synthesis.
816   *Traffic* 14: 2–14

817   Zhang K, Foster HE, Rondelet A, Lacey SE, Bahi-Buisson N, Bird AW, Carter AP (2017) Cryo-EM
818   Reveals How Human Cytoplasmic Dynein Is Auto-inhibited and Activated. *Cell* 169: 1303-
819   1314.e18

820   Zimyanin VL, Belaya K, Pecreaux J, Gilchrist MJ, Clark A, Davis I, St Johnston D (2008) In Vivo
821   Imaging of oskar mRNA Transport Reveals the Mechanism of Posterior Localization. *Cell* 134:
822   843–853

823

824   **MAIN FIGURES AND LEGENDS**

825   **Figure 1**
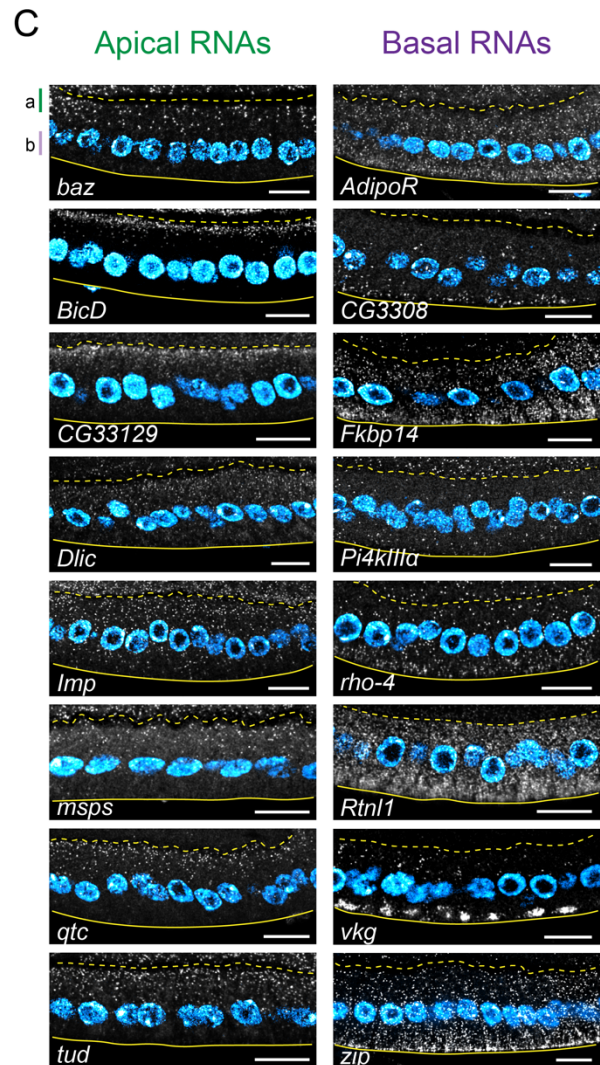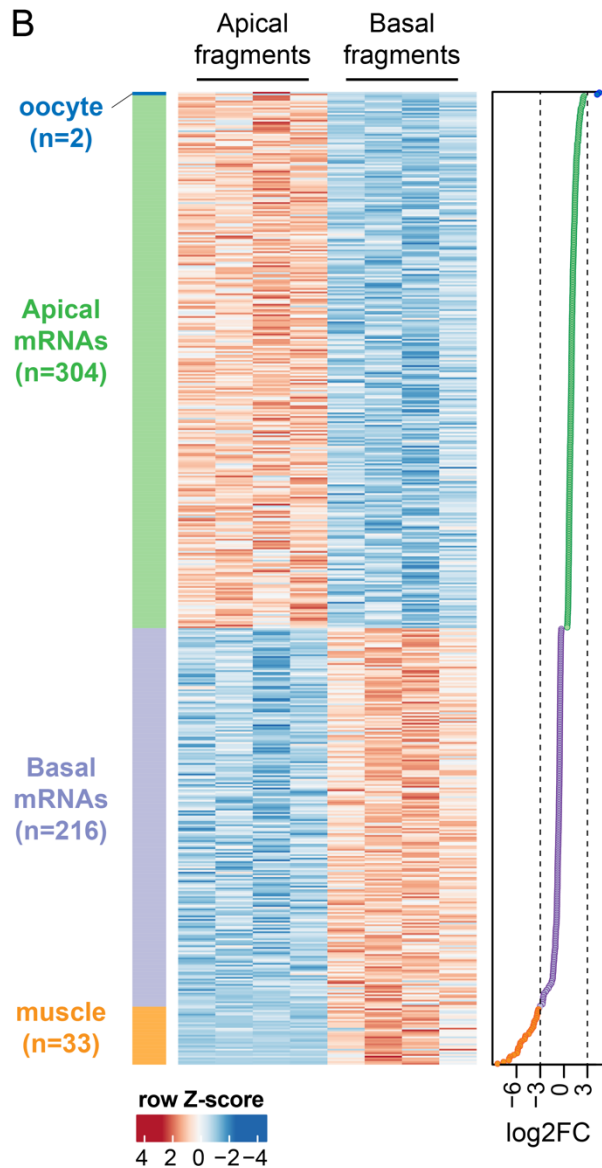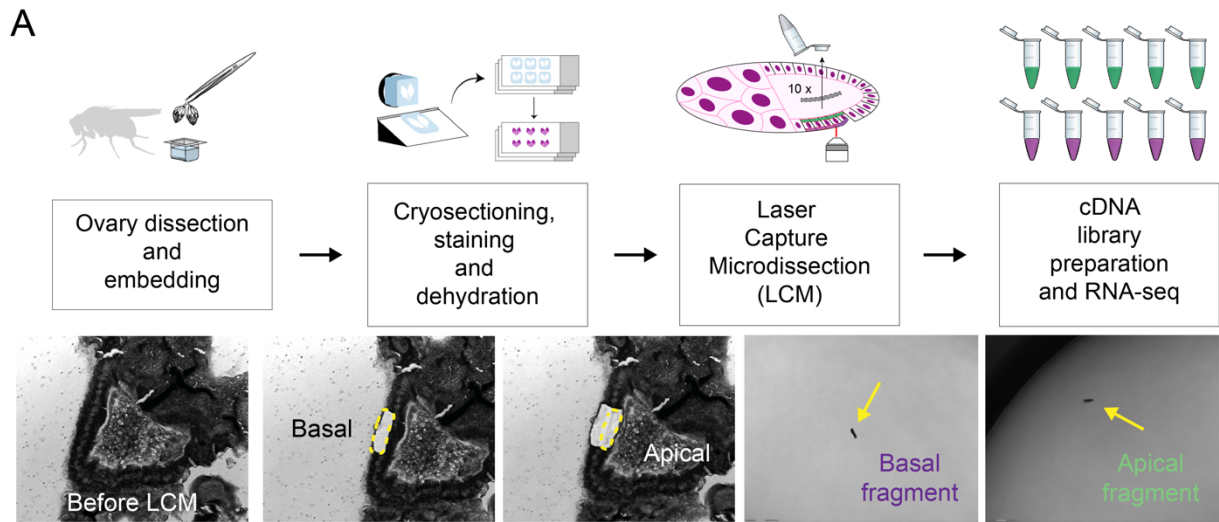
826

827 **Figure 1. Identification of apical and basal RNAs in *Drosophila* follicular epithelium by**

828 **subcellular spatial transcriptomics.** A) Schematic representation of the sample preparation

829 procedure. Lower panels: representative images of an egg chamber before and after apical and basal

830 fragment microdissection, including visualization of microdissected fragments in the cap of collection

831 tubes. B) Heatmap representing RNA-seq signal (*z*-score of normalized read counts) for significantly

832 enriched RNAs in microdissected apical and basal fragments (FDR < 0.1). Each row represents a

833 significantly enriched RNA in either apical samples (n=4) or basal samples (n=4). The log2FC value of

834 each RNA showed in the heatmap is indicated in the graph on the right. Dashed lines indicate

835 threshold log2FC values (log2FC < -3 and log2FC > 3) arbitrarily set to identify oocyte contaminants

836 (log2FC > 3, n=2, blue), *bona fide* apical RNAs (0 < log2FC ≤ 3, n=304, green), *bona fide* basal RNAs

837 (-3 ≤ log2FC < 0, n=216, purple), and muscle contaminants (log2FC ≤ -3, n=33, orange). C) smFISH

838 validation of 16 *bona fide* apical (left panels) and basal (right panels) RNAs. A dashed line and a

839 continuous line in each panel delimit the FC-oocyte and FC-basal lamina borders respectively. a =

840 apical domain; b = basal domain. Nuclei (cyan) are stained with DAPI. Scale bars 10 μm. See also

841 Figure S1, Table S1 and Video S1.

842

843

31

844   **Figure 2**
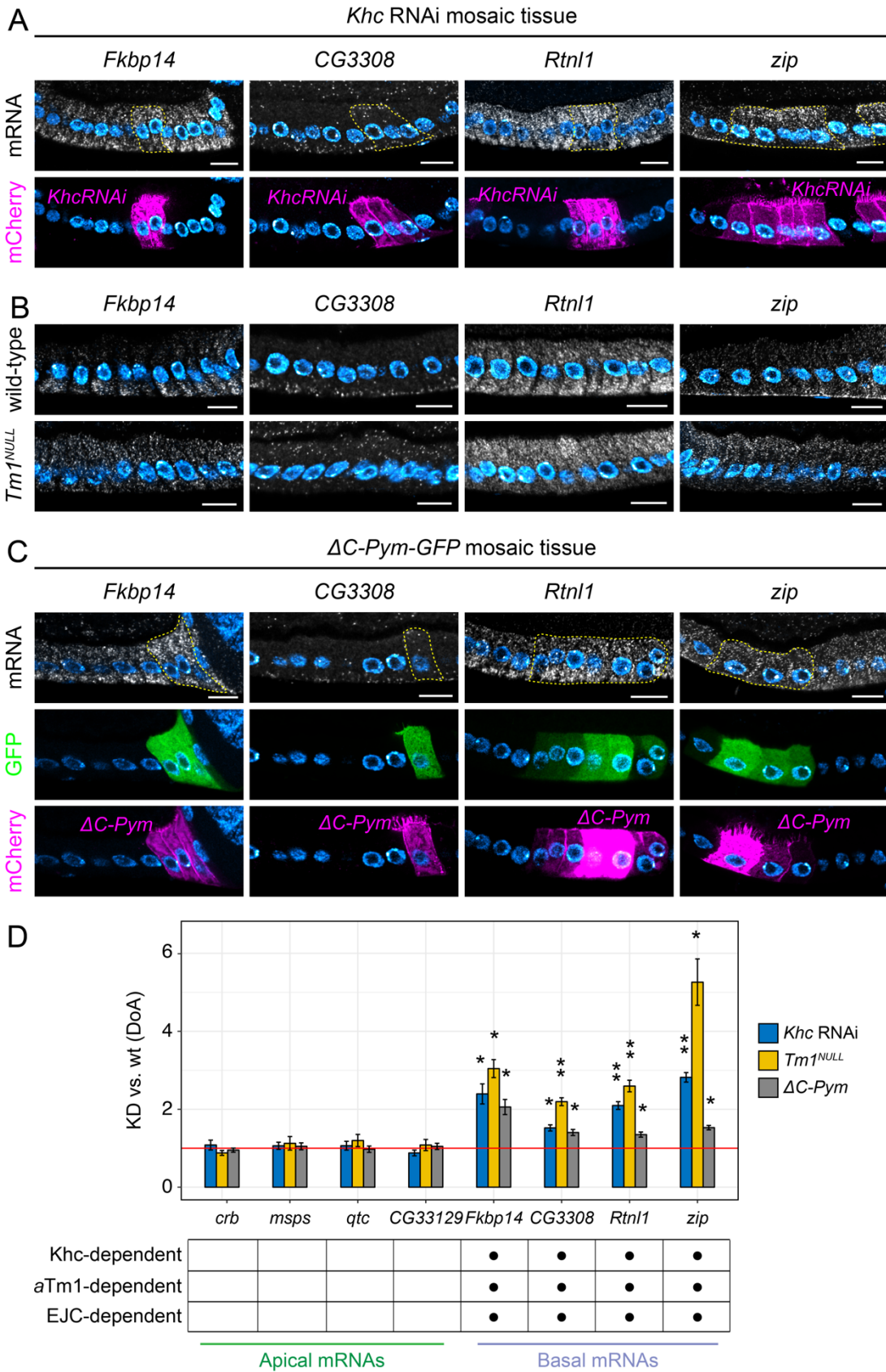
845

846

847 **Figure 2. Basal RNA localization depends on kinesin-1, *a*Tm1, and the EJC.**

848 In A) and C), mutant cells (marked with CD8-mCherry, lower panels) were generated by the UAS/Gal4

849 FLP-out system by inducing *Khc* RNAi (A) or by expressing the EJC-disrupting protein *ΔC-Pym* (C), to

850 disrupt each component without significantly affecting tissue architecture. Neighboring wild-type cells

851 are unmarked. A dashed line highlights mutant cells in smFISH images (upper panels). In B) the

852 expression of the *a*Tm1 isoform was specifically knocked down by generating *Tm1^{eg9}/Tm1^{eg1}*

853 (*Tm1^{NULL}*) egg chambers. A) Localization of basal RNAs by smFISH in *Khc* RNAi mosaic tissue. B)

854 Localization of basal RNAs by smFISH in wild-type and *Tm1^{NULL}* egg chambers. C) Localization of

855 basal RNAs by smFISH in *ΔC-Pym-GFP* mosaic tissue. D) Quantification of changes in the A-B

856 distribution of apical and basal RNAs in conditions of downregulated kinesin-1 transport. Analyzed

857 RNAs are indicated on the x-axis. The y-axis shows the average values (± s.e.m) of the ratio between

858 the Degree of Apicality (DoA) measured in knock-down (KD) cells and the DoA measured in wild-type

859 (wt) cells for each RNA analyzed, in each of the three conditions. The mean KD/wt(DoA) value for

860 each RNA in each condition was tested against a null hypothesis H_0 of KD/wt(DoA)=1 (red horizontal

861 line), corresponding to no change between mutant and wild-type cells (one-sample t-test). Asterisks

862 indicate mean values that significantly differ from the reference value of mu=1 (*=p<0.05; **=p<0.01;

863 ***=p<0.001). Nuclei (cyan) are stained with DAPI. Scale bars 10 µm. See also Figure S2 and Figure

864 S3.

865

866   **Figure 3**

867
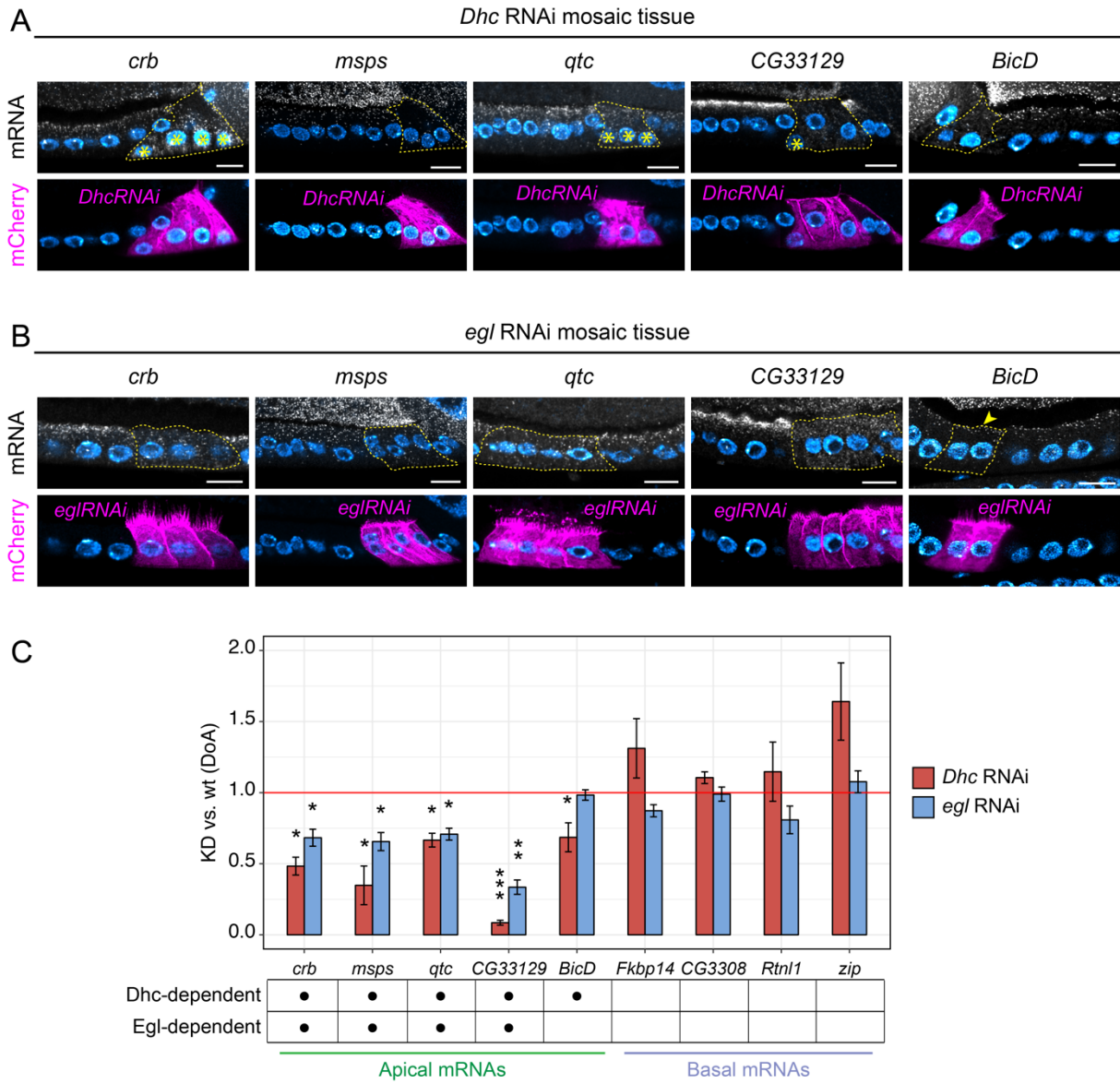
868

869

870 **Figure 3. Two different dynein-dependent mechanisms control apical RNA localization.**

871 A-B) Localization of apical RNAs by smFISH in *Dhc* RNAi (A) and *egl* RNAi mosaic tissue (B). Mutant

872 cells are marked by the expression of CD8-mCherry (lower panels) and highlighted with a dashed line

873 in smFISH images (upper panels). Neighboring wild-type cells are unmarked. Asterisks (*) indicate

874 basal mispositioning of nuclei due to *Dhc* RNAi, an indication of mild cell polarity defects. The

875 arrowhead in B) indicates the persistence of apical *BicD* RNA in *egl* RNAi cells. C) Quantification of

876 changes in the A-B distribution of apical and basal RNAs in conditions of downregulated

877 dynein/BicD/Egl transport (*Dhc* RNAi or *egl* RNAi). Analyzed RNAs are indicated on the x-axis. The y-

878 axis shows the average values ($\pm$ s.e.m) of the KD/wt ratio (DoA) for each RNA analyzed, in each of

879 the two conditions. The mean KD/wt(DoA) value for each RNA in each condition was tested against a

880 value of KD/wt(DoA)=1 (red horizontal line), corresponding to no change between mutant and wild-

881 type cells (one-sample t-test). Asterisks indicate mean values that significantly differ from the

882 reference value of mu=1 (*=$p<0.05$; **=$p<0.01$; ***=$p<0.001$). Nuclei (cyan) are stained with DAPI.

883 Scale bars 10 µm. See also Figure S4.

884
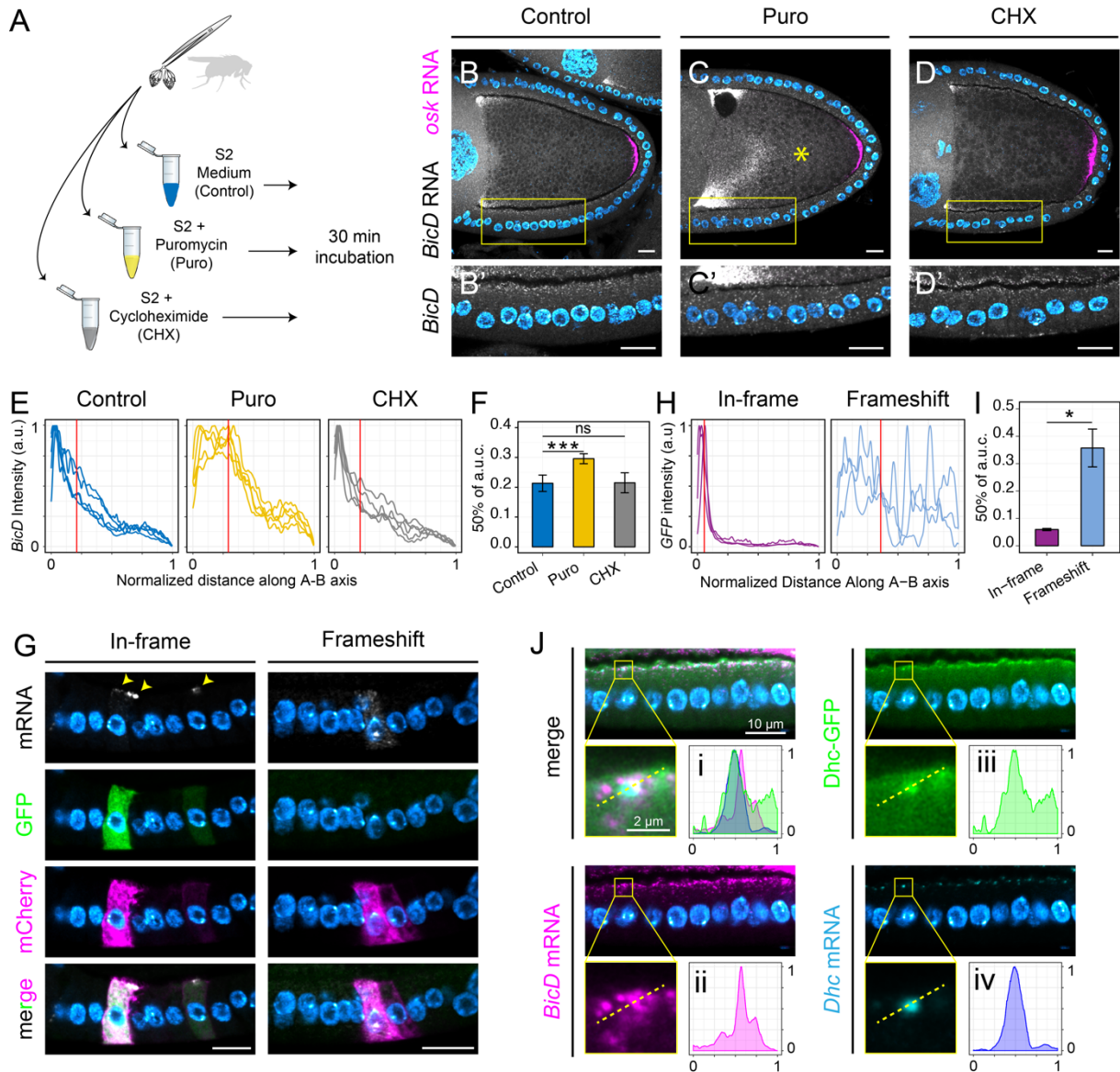
Figure 4

889   **Figure 4. *BicD* RNA is co-translationally localized at cortical Dhc foci.** A) Schematic

890   representation of the *ex vivo* treatment of wild-type ovaries with pharmacological inhibitors of

891   translation. B-D) Dual-color *BicD* (grayscale) and *osk* (magenta) smFISH experiments on Control (B-

892   B'), Puro- (C-C') or CHX-treated (D-D') ovaries. Insets show a magnification of the follicular epithelium

893   (bottom panels). Note the mislocalization of *BicD* RNA towards the center of the oocyte (*) in C). E)

894   Quantification of *BicD* RNA distribution along a linear ROI spanning the apical-basal axis of follicle

895   cells measured as smFISH fluorescence intensity in control (blue), Puro (yellow) and CHX (grey)

896   conditions. A red vertical line represents the mean x value corresponding to the 50% of the cumulative

897   area under the curve (a.u.c.), a proxy for *BicD* degree of mislocalization. F) Statistical analysis of *BicD*

898   degree of mislocalization (mean a.u.c. $\pm$ s.e.m) in each condition compared to control. Control-Puro:

899   p=0.000879 (***); Control-CHX: p=0.9374 (ns). G) Expression of different *BicD-GFP* constructs ("*In-*

900   *frame*": ^0BicD-*GFP*; "*Frameshift*": $^{(-1)}BicD$-*GFP* or $^{(+1)}BicD$-*GFP*) in FC clones and analysis of

901   transgenic RNA distribution by smFISH with antisense GFP probes. Follicle cell clones expressing

902   each *BicD-GFP* construct are marked by CD8-mCherry (magenta). H) Quantification of *In-frame*

903   (purple) or *Frameshift* (light blue) *BicD-GFP* RNA distribution. I) Statistical analysis of *BicD-GFP*

904   degree of mislocalization (mean a.u.c. $\pm$ s.e.m) in *Frameshift* compared to *In-frame* construct. p=

905   0.01719 (*). J) Localization of *BicD* RNA (magenta), *Dhc* RNA (cyan), and endogenously tagged Dhc-

906   GFP (green) in stage 10 follicular epithelium. Insets show a magnification of a single Dhc-GFP/*Dhc*

907   RNA focus. A dashed line indicates the cross-section along which each signal was measured (panels

908   i-iv). Signal intensities (y-axis) and line length (x-axis) were normalized in the 0-1 range. Nuclei (cyan)

909   are stained with DAPI. Scale bars 10 μm unless otherwise specified. See also Figure S5 and Figure

910   S6.

911

912 **Figure 5**

913
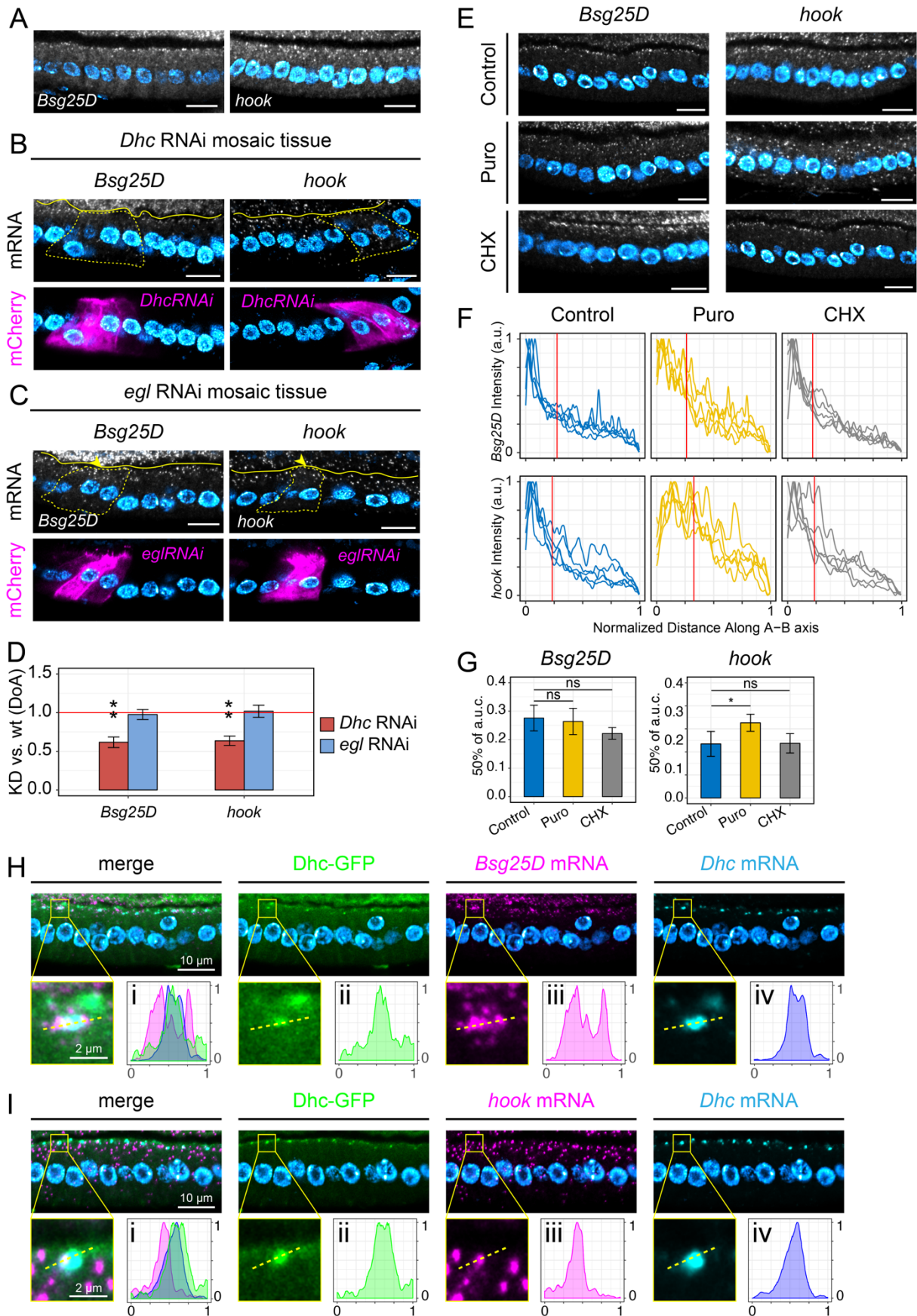
Figure 5. The apical localization of *hook* and *Bsg25D* RNAs is mechanistically similar to *BicD*.

A) *Bsg25D* and *hook* RNAs visualized by smFISH in wild-type FE. B-C) Localization of *Bsg25D* and *hook* RNAs by smFISH in *Dhc* RNAi (B) and *egl* RNAi mosaic tissue (C). Mutant cells are marked by the expression of CD8-mCherry (lower panels) and highlighted with a dashed line in smFISH images (upper panels). Neighboring wild-type cells are unmarked. Arrowheads in C) indicate the persistence of *Bsg25D* and *hook* RNAs apically in *egl* RNAi cells. A continuous yellow line demarcates the border between the oocyte and the FE to facilitate the image interpretation. D) Quantification of changes in the A-B distribution of *Bsg25D* and *hook* RNAs in conditions of downregulated dynein/BicD/Egl transport. The y-axis shows the average values ($\pm$ s.e.m) of the KD/wt DoA for each RNA analyzed, in each condition. The mean KD/wt DoA value for each RNA in each condition was tested against a value of KD/wt(DoA)=1 (red horizontal line). Asterisks indicate mean values that significantly differ from the reference value of mu=1 (*=$p<0.05$; **=$p<0.01$; ***=$p<0.001$). E) *Bsg25D* (left panels) and *hook* (right panels) RNA localization in the FE visualized by smFISH in Control, Puro- or CHX-treated ovaries. E) Quantification of *Bsg25D* (upper panels) and *hook* (lower panels) RNA distribution along linear ROIs spanning the apical-basal axis of follicle cells measured as smFISH fluorescence intensity in control (blue), Puro (yellow) and CHX (grey) conditions. A red vertical line represents the mean x value corresponding to 50% of each area under the curve (a.u.c.). G) Statistical analysis of *Bsg25D* and *hook* degree of mislocalization (mean a.u.c. $\pm$ s.e.m) in each condition compared to control. Control-Puro(*Bsg25D*): p= 0.6869 (ns); Control-CHX(*Bsg25D*): p=0.05405 (ns), Control-Puro(*hook*): p= 0.01648 (*); Control-CHX(*hook*): p= 0.9412 (ns). H-I) Localization of *Bsg25D* RNA (H) or *hook* RNA (I) (magenta), *Dhc* RNA (cyan), and endogenously tagged Dhc-GFP (green) in stage 10 follicular epithelium. Insets show a magnification of a single Dhc-GFP/*Dhc* RNA focus. A dashed line indicates the cross-section along which each signal has been measured (panels i-iv). Signal intensities (y-axis) and line length (x-axis) were normalized in the 0-1 range. Nuclei (cyan) are stained with DAPI. Scale bars 10 μm unless otherwise specified.

940   **Figure 6**

941
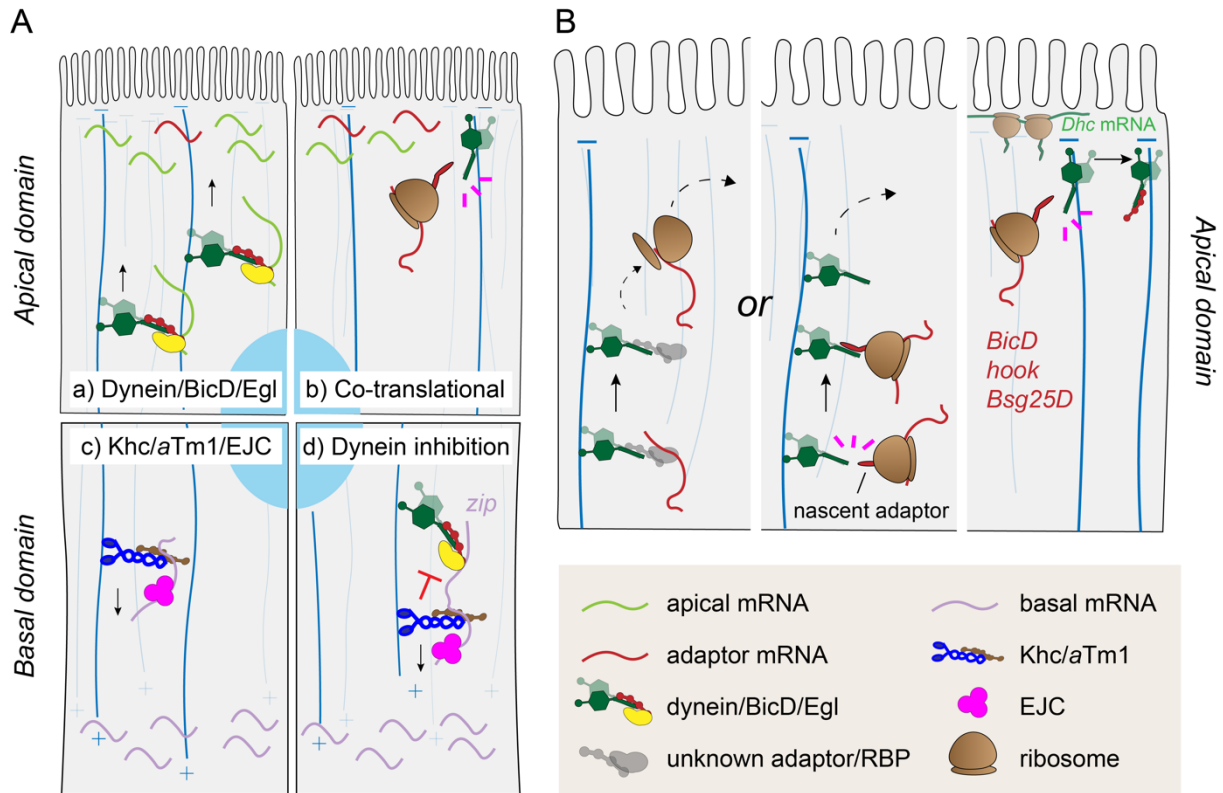
942

943

944

945 **Figure 6. Models of RNA localization mechanisms in follicle cells.** A) Model of the mechanism

946 underlying apical (a-b) and basal (c-d) RNA localization. Apical RNAs are localized at MT minus ends

947 by two dynein-dependent mechanisms: a) the dynein/BicD/Egl RNA transport machinery localizes

948 most of apical RNAs in the FE; b) a subset of dynein adaptors RNAs (*BicD*, *Bsg25D*, and *hook*)

949 localize co-translationally at cortical dynein foci. c) Basal RNAs are localized by Khc/*a*Tm1/EJC

950 moving towards MT plus ends enriched basally. d) In the transport of basal RNAs, the dynein complex

951 is kept in an inhibited state by kinesin-1 and its regulators. B) Model for the apical localization of

952 adaptor RNAs. RNAs can reach the apical domain by either canonical RNA transport by an unknown

953 RBP complex or by interaction of the nascent adaptor protein with dynein/dynactin transporting the

954 translationally engaged RNA to the apical domain. Once at the apical cortex, the nascent adaptor

955 associates through its N-terminal domain with newly translated cortically-anchored dynein, presumably

956 allowing the relief of both proteins' autoinhibition.

957